

Bubbles dynamics in microchannels: inertial and capillary migration forces

Rivero-Rodriguez, Javier¹† and Scheid, Benoit.¹

¹TIPs, Université Libre de Bruxelles, C.P. 165/67, Avenue F. D. Roosevelt 50, 1050 Bruxelles, Belgium

(Received xx; revised xx; accepted xx)

This work focuses on the dynamics of a train of unconfined bubbles flowing in microchannels. We investigate the transverse position of a train of bubbles, its velocity and the associated pressure drop when flowing in a microchannel depending on the internal forces due to viscosity, inertia and capillarity. Despite the small scales of the system, inertia, referred to as inertial migration force, play a crucial role in determining the transverse equilibrium position of the bubbles. Beside inertia and viscosity, other effects may also affect the transverse migration of bubbles such as the Marangoni surface stresses and the surface deformability. We look at the influence of surfactants in the limit of infinite Marangoni effect which yields rigid bubble interface. The resulting migration force may balance external body forces if present such as buoyancy, Dean or magnetic ones. This balance not only determines the transverse position of the bubbles but, consequently, the surrounding flow structure, which can be determinant for any mass/heat transfer process involved. Finally, we look at the influence of the bubble deformation on the equilibrium position and compare it to the inertial migration force at the centred position, explaining the stable or unstable character of this position accordingly. A systematic study of the influence of the parameters - such as the bubble size, uniform body force, Reynolds and capillary numbers - has been carried out using numerical simulations based on the Finite Element Method, solving the full steady Navier-Stokes equations and its asymptotic counterpart for the limits of small Reynolds and/or capillary numbers.

Key words: Microfluidics & Inertial migration & Capillary migration & Bubble dynamics

1. Introduction

Nowadays, microfluidic devices are increasingly used for fundamental and exploratory studies in chemistry and biology. Applications span from separation to dissolution processes including reactions which are all strongly coupled to bubble dynamics (Mikaelian *et al.* 2015*a,b*). In addition, the mixing (Günther *et al.* 2004) and mass transfer between the disperse and continuous phases (Mikaelian *et al.* 2015*a*) enhanced by flow recirculation patterns provide a good ambient for microreactions. Recently, bubble dissolution in microchannels has become of great interest for its application in CO_2 sequestration or reactants dissolution (Shim *et al.* 2014). In addition, micro-metric solid particles, drops, bubbles and more intricate objects such as capsules and cells can be easily manipulated with the help of a continuous phase. Continuous flow separation devices

† Email address for correspondence: jriveror@ulb.ac.be

rely on hydrodynamics forces, known as migration forces (Pamme 2007) and modulated either by the geometry - such as obstacles, patterns on the channel surface or varying channel section - or by body forces with gravitational, centrifugal, electrical, magnetic or acoustical origin.

Hydrodynamic forces have drawn the interest of the scientific community after the experiments of Segré & Silberberg (1962) on the migration of rigid spheres in Poiseuille flow with an inertial origin. Subsequently, a serie of experimental data (Tachibana 1973) was obtained in parallel with a theoretical background (Ho & Leal 1974; Schonberg & Hinch 1989) for rigid spheres. The effect of the particle rotation (Oliver 1962), the shear stress in linear profiles (Vasseur & Cox 1976; McLaughlin 1991) and the presence of a wall (Vasseur & Cox 1977) have also been addressed. Vasseur & Cox (1976) studied the dynamics of particles sedimenting in a stagnant fluid, shear flow and parabolic flow as well as the wall effect (Vasseur & Cox 1977). Inertial forces such as Dean ones have also been used to enhance cell ordering with applications to cell-in-droplet encapsulation (Kemna *et al.* 2012).

The effect of the particle size on its dynamics is a current field of research and, recently, the transition from small particle size to moderate size and the wall effect have been studied by Hood *et al.* (2015) showing the asymptotic behaviour for small particles. Differential behaviour with respect to particle size has been successfully exploited for particle sorting (Di Carlo *et al.* 2008). The influence of large Reynolds number flows on the transverse equilibrium positions has also been explored experimentally by Matas *et al.* (2004) showing different migration patterns depending on the Reynolds number.

One decade after the inertial migration was discovered, the migration force induced by the deformability of drops has been address by Chan & Leal (1979). The wall effect was shown by Kennedy *et al.* (1994) to be always repulsive. Numerical simulations on the transient evolution of capillary migration of large drops have been carried out by Coulliette & Pozrikidis (1998) and Mortazavi & Tryggvason (2000) who revealed that the stability of the centred positions of drops strongly depends on the viscosity ratio in the limit of small Reynolds numbers. Recently, experiments and transient simulations of deformable bubbles have been carried out by Chen *et al.* (2014) who considered also inertia and the joint effect of both. In this case, they showed how equilibrium positions move to the centerline as the increasing Reynolds number causes larger deformations. They also compared to inertial migration of rigid particles which is the limit of large inner to outer viscosity ratio.

On the other limit, small viscosity ratio represents the case of clean bubbles which has been studied. One can apply results in this limit to bubbles such as the wall effects found by Kennedy *et al.* (1994) whose repulsive character was confirmed in the case of bubbles by (Takemura *et al.* 2009) who studied the effect of the wall on bubbles rising close to it. Stan *et al.* (2011, 2013) described several mechanisms of migration of drops and bubbles in microchannels and focused on inertial an capillary migrations and carried out comparison between numerical and experimental results. They concluded that analytical theories of inertial (Ho & Leal 1974) and capillary (Chan & Leal 1979) migration do not provide a satisfactory quantitative prediction of migration forces and that the migration forces are very difficult to be measured experimentally. Despite these works, the dynamic of bubbles has caught less attention in the literature and a systematical study of the equilibrium state is required, especially in the presence of external force.

Migration forces have also been studied with more complex surface/bulk rheologies such as thermocapillary stresses (Subramanian 1983), Marangoni stresses with bulk-insoluble surfactant (Pak *et al.* 2014), for viscoelastic disperse media (Leshansky *et al.* 2007) and soft capsules (Singh *et al.* 2014).

The general problem of the transverse migration of particles, drops and bubbles has been addressed using several approaches such as experimental, analytical and numerical ones. As analytical approaches, regular asymptotic expansion for the Re numbers have been used in the inertial migration problem (Cox & Brenner 1968), together with matched asymptotic expansion in the bubble size, then limiting the solution to small particle/bubble sizes as well as sufficiently large separation between the bubble and the wall (Schonberg & Hinch 1989). Further, the transient evolution have been numerically computed using the Level Set Method (Stan *et al.* 2011; Yang *et al.* 2005) or using surface tracking methods, such as Arbitrary Lagrangian-Eulerian Method (Yang *et al.* 2005) or the Boundary Element Method (Zhou & Pozrikidis 1993). If the transient behaviour is not relevant, the equilibrium solution can be obtained skipping the transient evolution as performed by Mikaelian *et al.* (2015a). The latter approach allows, in terms of computational cost, systematic parametrical analysis.

In the literature, several mechanisms of the dynamics of particles, drops and bubbles have been explored with different techniques and in most of the cases, the dependence on the parameters governing the problem has been only qualitatively addressed, the main reasons being the computational cost of transient simulations, limitations of analytical techniques or experimental difficulties in the measurements of migration forces beside the relatively large number of parameters describing the problem. Even though asymptotic expansion has been addressed for the case of migration, the validity of its limits has not been reported. Also, direct comparison between inertial and capillary effects has been relatively unexplored as compared to their separate effects.

In this paper, we study inertial and capillary migrations in steady conditions in the presence of an external force in circular microchannels, i.e. a microchannel with a circular cross section. First, we write the governing equations which consist in the Navier-Stokes equations and no-slip boundary conditions at the walls of the channel, together with pseudo-periodic boundary conditions between the inlet and outlet section of a segment of the channel containing one bubble and moving at the velocity of the bubble. We consider rigid interface of the bubble, as well as stress-free boundary conditions both in the limit of undeformable bubbles and deformable bubbles with surface tension. We systematically explore the transverse equilibrium position depending on the Reynolds and capillary numbers, as well as the bubble size and uniform body force. We derive regular asymptotic expansion for small Reynolds and/or capillary numbers. The latter expansion involves the linearisation of boundary conditions applied at a deformed boundary and we propose a new approach for this task. We validate these expansions by comparison with the solution of the full system of equations and obtain the range of Reynolds and capillary numbers for which they are valid. We focus on both neutral bubbles, i.e. in absence of body force, and obtained their positions and stability and also explore the effect of the body force. The stability character of centred positions is also discussed. We finally studied the joint effect of inertia and capillary deformation on the equilibrium positions of neutral bubbles in the first-order expansion as well as the stability of centred bubbles in the full problem.

The structure of the paper is as follows. In sec. 2 we present the model we use to describe the dynamics of the train of bubbles of finite size and explain the underlying hypothesis. The boundary conditions at the bubble surface is given in sec. 2.1 for undeformable bubbles and in sec. 2.2 for deformable bubbles. Additional comments on the scaling and the numerics are given in sec. 2.3. In sec. 3.1 we study the effect of inertia, considering the limit of small Reynolds number and explore its range of validity. Analogously, in sec. 3.2 we investigate the effect of the deformation in the small capillary number limit and investigate its range of validity. In both cases, we focus on the neutral bubbles

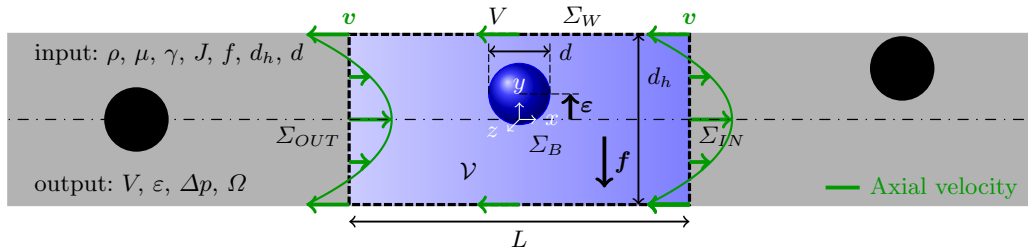


FIGURE 1. Sketch of the modelled segment of a train of bubble in a microchannel.

as a reference and the stability of the centred position, as well as the effect of the body force. We complete our study, comparing inertial and capillary effects around the centred position solving the full problem and recovering the small Re and Ca number limits in sec. 3.3. Conclusions are presented in sec. 4.

2. Modelling

We model the dynamics of a train of bubbles in a circular microchannel. Different equilibrium positions are possible depending on the bubble size and on the balance of several forces such as viscous, inertial, capillary and body forces. To model this situation, we consider a volume \mathcal{V} containing one bubble attached to it and delimited by the walls of the channel, Σ_W , two cross sections of the channel, Σ_{IN} and Σ_{OUT} , and the surface of the bubble, Σ_B , as schematised in fig. 1b. It is assumed that the characteristic time in which changes of volume of the bubble occur, either due to dissolution or due to the compressibility of the gas, is small compared to the residence time (Mikaelian *et al.* 2015*a,b*) and, therefore, the evolution of the bubble can be considered as quasi-steady in absence of neither vortex shedding nor turbulence, as considered in this work. We include the influence of a uniform body force $\mathbf{f} = f\mathbf{e}_y$ (for gravity $f = -\rho g$) in the transverse direction. A liquid of density ρ , viscosity μ and surface tension γ flows inside a channel of hydraulic diameter d_h with a mean velocity J producing a pressure drop due to the Poiseuille flow modified by the presence of one bubble, Δp , among a segment of length L taken sufficiently large to avoid bubbles from interfering with each other. The bubble travels with a velocity V and with centre at $\varepsilon = \varepsilon\mathbf{e}_y$ where the eccentricity ε is measured from the centre of the channel and determined by the balance of forces acting on the bubble surface in the transverse direction. The bubble might eventually rotate. Pseudo-periodic boundary conditions are considered in the 'IN' and 'OUT' cross sections, velocity V is imposed at the walls of the channels such that the frame of reference is moving with the bubble. The velocity of the bubble is determined by the balance of forces acting on the bubble surface in the streamwise direction. Two different conditions are considered at the surface of the bubbles, either stress-free or rigid. In the former case, capillary deformation of the bubble will also be investigated.

According to the previous description, the liquid flow around the bubble in the modelled segment of channel can be analysed by solving, in the reference frame attached to the bubble, the continuity and the steady Navier-Stokes equations,

$$\nabla \cdot \mathbf{v} = 0 \quad \text{at } \mathcal{V}, \quad (2.1a)$$

$$\rho \mathbf{v} \cdot \nabla \mathbf{v} = -\nabla \hat{p} + \nabla \cdot \boldsymbol{\tau} \quad \text{at } \mathcal{V}, \quad (2.1b)$$

where \hat{p} , \mathbf{v} and $\boldsymbol{\tau} = \frac{1}{2}\mu[\nabla \mathbf{v} + (\nabla \mathbf{v})^T]$ are the reduced pressure, the velocity and the

viscous stress tensor, respectively. The pressure then writes as $p = \hat{p} + \mathbf{f} \cdot (\mathbf{x} - \boldsymbol{\varepsilon})$ with pressure reference chosen at the centre of the bubble without loss of generality.

Since we consider the reference frame attached to the bubble moving at the equilibrium velocity, V , no net force is applied on it in the x -direction because the body force is applied in the orthogonal (transverse) direction only. Therefore, the boundary condition at the wall is

$$\mathbf{v}(\mathbf{x}) = -V\mathbf{e}_x \quad \text{at } \Sigma_W, \quad (2.2)$$

while the equilibrium condition for the bubble is

$$\int_{\Sigma_B} \mathbf{e}_x \cdot (-\hat{p}\mathcal{I} + \boldsymbol{\tau}) \cdot \mathbf{n} \, d\Sigma = \int_{\Sigma_B} \mathbf{f} \cdot (\mathbf{x} - \boldsymbol{\varepsilon})\mathbf{e}_x \cdot \mathbf{n} \, d\Sigma, \quad (2.3)$$

where \mathbf{n} and $d\Sigma$ are the outer normal and the differential surface, respectively.

Next, pseudo-periodic boundary conditions, that relate the velocity and the pressure at the inlet, Σ_{IN} , and at the outlet, Σ_{OUT} , of the channel, are

$$\hat{p}(\mathbf{x} + L\mathbf{e}_x) = \hat{p}(\mathbf{x}) - \Delta p + L\partial_x p_P \quad \text{at } \Sigma_{OUT}, \quad (2.4a)$$

$$\mathbf{v}(\mathbf{x} + L\mathbf{e}_x) = \mathbf{v}(\mathbf{x}) \quad \text{at } \Sigma_{OUT}, \quad (2.4b)$$

$$\partial_x \mathbf{v}(\mathbf{x} + L\mathbf{e}_x) = \partial_x \mathbf{v}(\mathbf{x}) \quad \text{at } \Sigma_{OUT}, \quad (2.4c)$$

and accommodate the pressure drop due to the Poiseuille flow $\partial_x p_P = -32\mu J/d_h^2$ modified by the pressure drop Δp due to the presence of the bubble. The mean flow rate J is then imposed by

$$\int_{\Sigma_{IN}} (\mathbf{v} \cdot \mathbf{e}_x + V - J) \, d\Sigma = 0. \quad (2.5)$$

The averaged pressure drop per unit length, $\Delta_x p_T$, produced in a microchannel of length ℓ containing N bubbles of size d at equilibrium positions $\boldsymbol{\varepsilon}$ fulfils $\ell\Delta_x p_T = \ell\partial_x p_P - N\Delta p(\boldsymbol{\varepsilon}, d)$, where N is related to the bubble volumetric fraction $\alpha_G = N\mathcal{V}_B/\ell\Sigma_{IN}$, the volume of the bubble $\mathcal{V}_B = \frac{\pi}{6}d^3$ and the microchannel cross section $\Sigma_{IN} = \frac{\pi}{4}d_h^2$. Thus, the averaged pressure writes

$$\frac{\Delta_x p_T}{\partial_x p_P} = 1 + \beta\alpha_G, \quad (2.6)$$

where β is the pressure correction factor $\beta = -\Sigma_{IN}\Delta p/\mathcal{V}_B\partial_x p_P$ and the geometrical factor is $\Sigma_{IN}/\mathcal{V}_B = 3d_h^2/2d^3$ in circular microchannels. (2.6) has been experimentally observed by Cubaud & Ho (2004) in the limit of small α_G in square microchannels with a wide dispersion around the value $\beta = 1$ which may be due to the actual dependence of the bubble size and eccentricity. In fact, β spans from negative to positive values as $\Delta p(\boldsymbol{\varepsilon}, d)$ does.

We consider different boundary conditions at the surface of the bubble depending on if the capillary deformation of the bubble is taken into account.

2.1. Undeformable bubbles

Firstly, we consider rigid and stress-free boundary conditions on the surface of undeformed bubble. It is relevant for the study of the inertial migration in the cases of infinite Marangoni effect and clean surface, respectively.

On the one hand, in the limit of infinite Marangoni effect, the flow at the bubble surface corresponds to that of a rigid solid that rotates with rotational velocity $\boldsymbol{\Omega}$ which turns out to be in the z -direction, $\boldsymbol{\Omega} = \Omega\mathbf{e}_z$, and is determined by the no-slip condition

and by the equilibrium of moments, respectively,

$$\mathbf{v}(\mathbf{x}) = \boldsymbol{\Omega} \times (\mathbf{x} - \boldsymbol{\varepsilon}) \quad \text{at } \Sigma_B, \quad (2.7a)$$

$$\mathbf{0} = \int_{\Sigma_B} (\mathbf{x} - \boldsymbol{\varepsilon}) \times \boldsymbol{\tau} \cdot \mathbf{n} \, d\Sigma. \quad (2.7b)$$

These conditions also correspond to the case of infinitely viscous drops or equivalently to solid spheres.

On the other hand, in the case of clean bubbles, the stress-free boundary condition and the impermeability condition are applied for the case of clean bubbles, i.e.

$$(-\hat{p}\mathcal{I} + \boldsymbol{\tau}) \cdot \mathbf{n} = -\hat{\lambda}\mathbf{n} \quad \text{at } \Sigma_B, \quad (2.8a)$$

$$\mathbf{v} \cdot \mathbf{n} = 0 \quad \text{at } \Sigma_B, \quad (2.8b)$$

where the surface variable $\hat{\lambda}$ is the reduced counterpart of the 'contact' pressure $\lambda = \hat{\lambda} + \mathbf{f} \cdot (\mathbf{x} - \boldsymbol{\varepsilon})$ that ensures the impermeability. It is worth mentioning that these boundary conditions also correspond to the case of inviscid drops.

Note that, the RHS of (2.3) vanishes if \mathbf{f} has no component in the x -direction, as considered. Therefore, \mathbf{f} does not enter explicitly in (2.1)-(2.8) and it is numerically convenient to use f as unknown and consider $\boldsymbol{\varepsilon}$ as a priori given, instead. In this way, the domain will also be a priori given. Then, if one defines the migration force as the force that the liquid exert on the bubble in absence of outer force in the transverse direction y ,

$$\mathcal{L} = - \int_{\Sigma_B} \mathbf{e}_y \cdot (-\hat{p}\mathcal{I} + \boldsymbol{\tau}) \cdot \mathbf{n} \, d\Sigma, \quad (2.9)$$

the body force f can be obtained from the transverse balance of forces exerted on the bubble, $\int_{\Sigma_B} \mathbf{e}_y \cdot (-\hat{p}\mathcal{I} + \boldsymbol{\tau}) \cdot \mathbf{n} \, d\Sigma = 0$. In effect, the balance of migration force and body force writes

$$\mathcal{L} = \frac{\pi}{6} d^3 f. \quad (2.10)$$

Thus, we equivalently refer hereafter to the balanced body force, f , instead of the migration force, \mathcal{L} , it is in equilibrium with.

2.2. Deformable bubbles

Secondly, we consider the case of deformable bubbles which is relevant for the study of the capillary migration. In this case the surface position is governed by the following equilibrium of stresses and the impermeability condition

$$\mathbf{n} \cdot \{[-\hat{p} - \mathbf{f} \cdot (\mathbf{x} - \boldsymbol{\varepsilon}) + p_G]\mathcal{I} + \boldsymbol{\tau}\} = \hat{\nabla}_S \gamma \quad \text{at } \Sigma_B, \quad (2.11a)$$

$$\mathbf{v} \cdot \mathbf{n} = 0 \quad \text{at } \Sigma_B, \quad (2.11b)$$

where p_G is the gas pressure governed by the Young-Laplace law and the surface operator $\hat{\nabla}_S$ is defined by its application to a quantity φ as $\hat{\nabla}_S \varphi = \nabla \cdot (\mathcal{I}_S \varphi)$ and \mathcal{I}_S is the surface identity tensor, i.e. $\mathcal{I}_S = \mathcal{I} - \mathbf{nn}$ with \mathbf{nn} the dyadic product. Note that we only consider constant γ , i.e. no finite Marangoni stress. Nevertheless, in this case, p_G and \mathbf{f} appear explicitly in (2.11a). Both quantities, which are a priori unknown, are related to the

volume of the bubble and its position, respectively,

$$\frac{\pi}{6}d^3 = \int_{\mathcal{V}_B} d\mathcal{V}, \quad (2.12a)$$

$$\mathbf{0} = \int_{\mathcal{V}_B} (\mathbf{x} - \boldsymbol{\varepsilon}) d\mathcal{V}, \quad (2.12b)$$

where \mathcal{V}_B is the domain occupied by the bubble. Note that (2.3) is the x -projection of the integral of (2.11a) among the bubble surface and, therefore, redundant. The transverse projection of (2.12b) represents the equation for the transverse body force whereas the longitudinal projection represents the equation for the velocity of the bubble.

2.3. Scaling and numerics

It is worth noting that the system of equations (2.1)-(2.12) involve domain variables \hat{p} and \mathbf{v} , surface variables $\hat{\lambda}$ and global variables f , V , Δp , Ω and p_G . This system of equations can be made dimensionless with the hydraulic diameter of the channel d_h , the mean velocity of the flow J and the viscous stress $\mu J/d_h$ as characteristic length, velocity and pressure, respectively. In particular, the substitution in the equations of

$$d_h \rightarrow 1, \quad J \rightarrow 1, \quad \mu \rightarrow 1, \quad \rho \rightarrow Re, \quad \gamma \rightarrow Ca^{-1}, \quad \varepsilon \rightarrow \tilde{\varepsilon}, \quad d \rightarrow \tilde{d}, \quad (2.13)$$

leads to the dimensionless formulation with the dimensionless numbers

$$Re = \frac{\rho J d_h}{\mu}, \quad Ca = \frac{\mu J}{\gamma}, \quad \tilde{\varepsilon} = \frac{\varepsilon}{d_h}, \quad \tilde{d} = \frac{d}{d_h}, \quad (2.14)$$

the dimensionless domain variables

$$\tilde{\mathbf{v}} = \frac{\mathbf{v}}{J}, \quad \tilde{p} = \frac{\hat{p} d_h}{\mu J}, \quad (2.15)$$

and dimensionless global variables

$$\tilde{\mathcal{L}} = \frac{\mathcal{L}}{\mu J d_h}, \quad \tilde{V} = \frac{V}{J}, \quad \Delta \tilde{p} = \frac{\Delta p d_h}{\mu J}, \quad \tilde{\Omega} = \frac{\Omega d_h}{J}, \quad (2.16)$$

or alternatively β and $\tilde{f} = f d_h^2 / \mu J$, instead of $\Delta \tilde{p}$ and \tilde{f} , respectively. Typical values for water in a microchannel of diameter $d_h = 500 \mu\text{m}$ and a flow rate of $J = 0.1 \text{ m/s}$ correspond to dimensionless numbers of $Re = 50$ and $Ca = 1.4 \cdot 10^{-3}$. Tildes are removed in the following for the sake of clarity.

The dimensionless counterpart of the system of equations (2.1)-(2.12) is solved using the Finite Element Method. The equations are implemented in weak form using the software COMSOL and deformation of the surface is considered using the Arbitrary Lagrangian-Eulerian method which are implemented in the *Moving Mesh* module. We have validated the implementation of the previous equations by comparing the equilibrium position of a particle with diameter $d = 0.305$ for $Re = 0.196$, in absence of body force, obtained by other authors both numerically and experimentally, see figure 2 in Yang *et al.* (2005). We benefit of the symmetry with respect to the $z = 0$ plane to reduce by a factor 2 the mesh size although computational time -which remains within the range of a few minutes (1-3 minutes) for one solution- is not limiting in the computations reported here. We have also carefully checked the convergence of a tetrahedral mesh with hexahedral elements on the bubble surface. Symmetric meshes with respect to the $x = 0$ plane has been found to increase the accuracy on the solution.

| | \parallel | Re | Ca | Expansion | Symmetries & reversibilities |
|-----------------------------------|-------------|--------------|--------------|--------------|------------------------------|
| Leading order creeping flow | \parallel | 0 | 0 | zeroth order | AS & R |
| Pure linear inertial flow | \parallel | $Re < Re_*$ | 0 | first order | S & AR |
| Pure linear capillary flow | \parallel | 0 | $Ca < Ca_*$ | first order | S & AR |
| Pure nonlinear inertial flow | \parallel | $\forall Re$ | 0 | full | none |
| Pure nonlinear capillary flow | \parallel | 0 | $\forall Ca$ | full | none |
| Linear inertial-capillary flow | \parallel | $Re < Re_*$ | $Ca < Ca_*$ | first order | S & AR |
| Nonlinear inertial-capillary flow | \parallel | $\forall Re$ | $\forall Ca$ | full | none |

TABLE 1. Considered flows involving inertial and capillary migrations. S: symmetric, AS: anti-symmetric, R: reversible and AR: anti-reversible (see app. B for definitions).

3. Migration forces

In this section, we investigate both inertial and capillary migration forces. First, we quantitatively study the influence of the size of the bubble and the eccentricity (body force) in the limit of small Re or Ca numbers, separately. Asymptotic regular expansions are derived for these limits in dimensionless form which lead to the creeping flow around undeformed spheres for zeroth order and the inertial or capillary perturbations for first order. Their range of validity are studied by solving the nonlinear full problem (2.1)-(2.12) and a criteria is obtained depending on the bubble diameter, i.e. $Re < Re_*(d)$ or $Ca < Ca_*(d)$. The stability of the centred position, namely $\varepsilon = 0$, is studied using both limits and again comparing with the solution of the full problem. All cases are summarised in table 1 where we also include the symmetric and reversible features exhibited by the flow around the $x = 0$ plane, the details of which are given in the app. B.

3.1. Inertial migration.

Straight channels are a particular geometry in which a constant flow does not depend on the Reynolds number provided no turbulence develops and it corresponds to the purely creeping flow which is reversible. However, the presence of the bubble modifies the flow structure in such a manner that inertia forces come into play and, thus, break the reversibility of the flow. In this case, the bubble experience a transverse force with inertial origin even for small but finite inertia (Segré & Silberberg 1962). It motivates an expansion of the system of equations (2.1)-(2.10) for small Reynolds number as $\psi = \sum_{j=0}^{\infty} Re^j \psi_j$, where ψ represents any of the dependent variables \hat{p} , \mathbf{v} , f , V , Δp or $\hat{\lambda}$ and Ω (if applicable), that yields (Cox & Brenner 1968), up to first order, to

$$\nabla \cdot \mathbf{v}_0 = 0, \quad \nabla \cdot \mathbf{v}_1 = 0 \quad \text{at } \mathcal{V}, \quad (3.1a)$$

$$\mathbf{0} = \nabla \cdot (-\hat{p}_0 \mathcal{I} + \boldsymbol{\tau}_0), \quad \mathbf{v}_0 \cdot \nabla \mathbf{v}_0 = \nabla \cdot (-\hat{p}_1 \mathcal{I} + \boldsymbol{\tau}_1) \quad \text{at } \mathcal{V}, \quad (3.1b)$$

together with the perturbation of the velocity at the walls

$$\mathbf{v}_0(\mathbf{x}) = -V_0 \mathbf{e}_x, \quad \mathbf{v}_1(\mathbf{x}) = -V_1 \mathbf{e}_x \quad \text{at } \Sigma_W, \quad (3.2)$$

of the equilibrium equations for the bubble

$$0 = \int_{\Sigma_B} \mathbf{e}_x \cdot (-\hat{p}_0 \mathcal{I} + \boldsymbol{\tau}_0) \cdot \mathbf{n} \, d\Sigma, \quad 0 = \int_{\Sigma_B} \mathbf{e}_x \cdot (-\hat{p}_1 \mathcal{I} + \boldsymbol{\tau}_1) \cdot \mathbf{n} \, d\Sigma, \quad (3.3)$$

and of the pseudo-periodic conditions

$$\hat{p}_0(\mathbf{x} + L\mathbf{e}_x) = \hat{p}_0(\mathbf{x}) - \Delta p_0 + L\partial_x p_P, \quad \hat{p}_1(\mathbf{x} + L\mathbf{e}_x) = \hat{p}_1(\mathbf{x}) - \Delta p_1 \quad \text{at } \Sigma_{OUT}, \quad (3.4a)$$

$$\mathbf{v}_0(\mathbf{x} + L\mathbf{e}_x) = \mathbf{v}_0(\mathbf{x}), \quad \mathbf{v}_1(\mathbf{x} + L\mathbf{e}_x) = \mathbf{v}_1(\mathbf{x}) \quad \text{at } \Sigma_{OUT}, \quad (3.4b)$$

$$\partial_x \mathbf{v}_0(\mathbf{x} + L\mathbf{e}_x) = \partial_x \mathbf{v}_0(\mathbf{x}), \quad \partial_x \mathbf{v}_1(\mathbf{x} + L\mathbf{e}_x) = \partial_x \mathbf{v}_1(\mathbf{x}) \quad \text{at } \Sigma_{OUT}, \quad (3.4c)$$

which accommodate the flow rate

$$\int_{\Sigma_{IN}} (\mathbf{v}_0 \cdot \mathbf{e}_x + V_0 - 1) \, d\Sigma = 0, \quad \int_{\Sigma_{IN}} (\mathbf{v}_1 \cdot \mathbf{e}_x + V_1) \, d\Sigma = 0. \quad (3.5)$$

The boundary conditions on the bubble surface are

$$\mathbf{v}_0(\mathbf{x}) = \boldsymbol{\Omega}_0 \times (\mathbf{x} - \boldsymbol{\varepsilon}), \quad \mathbf{v}_1(\mathbf{x}) = \boldsymbol{\Omega}_1 \times (\mathbf{x} - \boldsymbol{\varepsilon}) \quad \text{at } \Sigma_B, \quad (3.6a)$$

$$\mathbf{0} = \int_{\Sigma_B} (\mathbf{x} - \boldsymbol{\varepsilon}) \times \boldsymbol{\tau}_0 \cdot \mathbf{n} \, d\Sigma, \quad \mathbf{0} = \int_{\Sigma_B} (\mathbf{x} - \boldsymbol{\varepsilon}) \times \boldsymbol{\tau}_1 \cdot \mathbf{n} \, d\Sigma, \quad (3.6b)$$

at the rigid interface, or

$$(-\hat{p}_0 \mathcal{I} + \boldsymbol{\tau}_0) \cdot \mathbf{n} = -\hat{\lambda}_0 \mathbf{n}, \quad (-\hat{p}_1 \mathcal{I} + \boldsymbol{\tau}_1) \cdot \mathbf{n} = -\hat{\lambda}_1 \mathbf{n} \quad \text{at } \Sigma_B, \quad (3.7a)$$

$$\mathbf{v}_0 \cdot \mathbf{n} = 0, \quad \mathbf{v}_1 \cdot \mathbf{n} = 0 \quad \text{at } \Sigma_B, \quad (3.7b)$$

at the stress-free interface. The perturbation of the inertial migration force defined by (2.9) writes

$$\mathcal{L}_0 = - \int_{\Sigma_B} \mathbf{e}_y \cdot (-\hat{p}_0 \mathcal{I} + \boldsymbol{\tau}_0) \cdot \mathbf{n} \, d\Sigma, \quad \mathcal{L}_1 = - \int_{\Sigma_B} \mathbf{e}_y \cdot (-\hat{p}_1 \mathcal{I} + \boldsymbol{\tau}_1) \cdot \mathbf{n} \, d\Sigma. \quad (3.8)$$

Note that the migration force can be alternatively computed using the reciprocal theorem as performed by Ho & Leal (1974).

The solution of the system (3.1)-(3.8) for the migration force, velocity of the bubble, pressure drop and rotational velocity (only applicable in the case of rigid interface) is of the form

$$f_\rho \equiv \frac{f}{Re} \approx f_1(\varepsilon, d), \quad V \approx V_0(\varepsilon, d), \quad \beta \approx \beta_0(\varepsilon, d), \quad \Omega \approx \Omega_0(\varepsilon, d), \quad (3.9)$$

where the removed terms have been found numerically to be vanishing, i.e. $f_0 = V_1 = \beta_1 = \Omega_1 = 0$ as it can be inferred from the symmetries and reversibilities of the flow. Consequently, the balanced body force comes from the first-order solution whereas the velocity, pressure correction factor and the rotational velocity comes from the zeroth-order solution.

In fig. 2, we depict the solution (3.9) for a representative bubble of size $d = 0.4$ in the small Reynolds number limit for values of eccentricity within the geometrically feasible range $-\varepsilon_* < \varepsilon < \varepsilon_*$ where $\varepsilon_* = \frac{1}{2}(1 - d)$ corresponds to the position of bubbles touching the wall. In fig. 2a, we can observe the existence of multiple equilibrium positions of the bubble for a range of values of the balanced body force f and this multiplicity of solutions is lost for sufficiently large values of the balanced body force and for which the bubbles are closer to the wall. In particular, for the case of neutral bubbles, i.e. no body force, $f = 0$, there exists typically three equilibrium solutions, whose stability is determined by the slope $\partial_\varepsilon f$, two of them being stable, denoted by (i) and (iii), whose attraction ranges

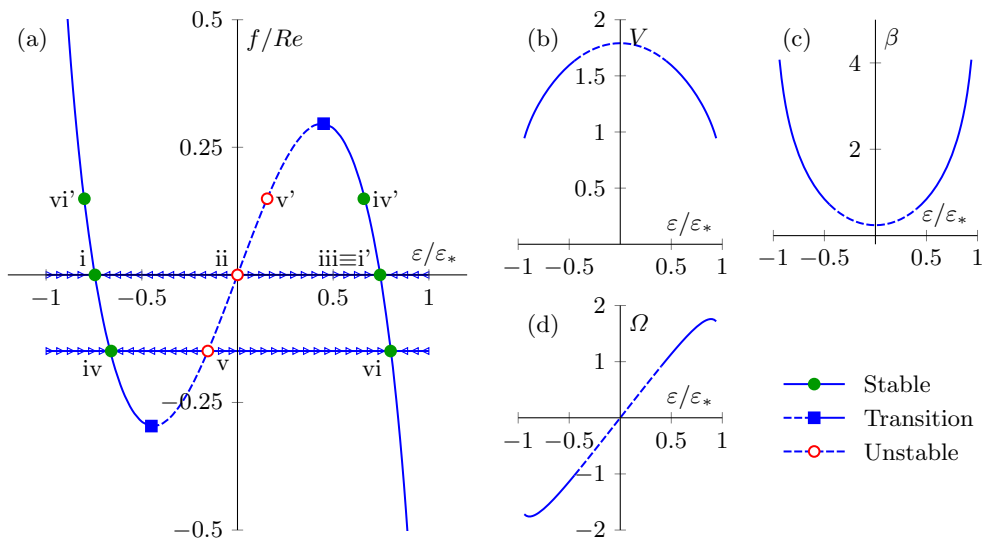


FIGURE 2. Effect of the eccentricity ε of bubbles with rigid interface and size $d = 0.4$ in the pure linear inertial regime on the (a) balanced body force, (b) velocity of the bubble, (c) pressure correction factor and (d) rotational velocity.

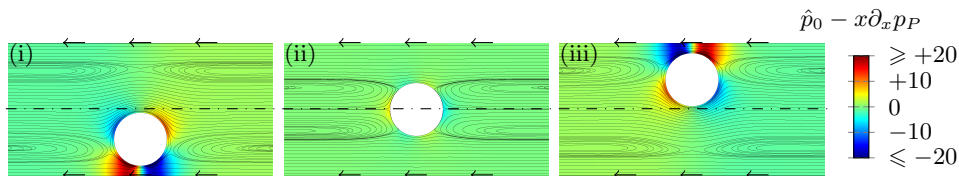


FIGURE 3. Streamlines of the creeping flow, \mathbf{v}_0 , and colormap for the pressure field, $\hat{p}_0 - x \Delta_x p_P$, of the creeping flow at the symmetry plane $z = 0$ for neutral bubbles with rigid interface and size $d = 0.4$. Labels corresponds to points in fig. 2a.

are separated by the unstable one (ii). It is represented by the line decorated with arrows indicating the transverse motion of a bubble when located out of the equilibrium position. On the one hand, this can be observed by turning the force on towards negative value but moderate so that multiple solutions still exist, namely $f/Re = -0.15$. In effect it results in a positive force exerted on the bubbles and, therefore, bubbles at stable positions, namely in the position (i) and (iii), are shifted upward toward positions (iv) and (vi), i.e. in the same direction than the force exerted on the bubble, namely to the right in fig. 2a. Unstable bubbles, namely at position (ii), are shifted in the opposite direction towards (v), revealing the unstable character of this position. Analogous reasons show that the positions (iv)-(vi) show the same character than (i)-(iii). Once the equilibrium position for a given body force f is known, one can obtain from fig. 2b-d the values of V , Δp and Ω . In effect, at the centre of the channel, i.e. $\varepsilon = 0$, the velocity of the bubble is maximal, the pressure drop is minimal and the rotational velocity reverses orientation. Observe the symmetries of the functions in (3.9) with respect to the position of the bubble, it is sufficient to explain them only for positive eccentricities, $\varepsilon \geq 0$. Note the odd symmetry of the balance body force for which any condition has an equivalent for the opposite position, for instance denoted with the same roman number and an apostrophe in the case of moderate and positive force, $f/Re = +0.15$.

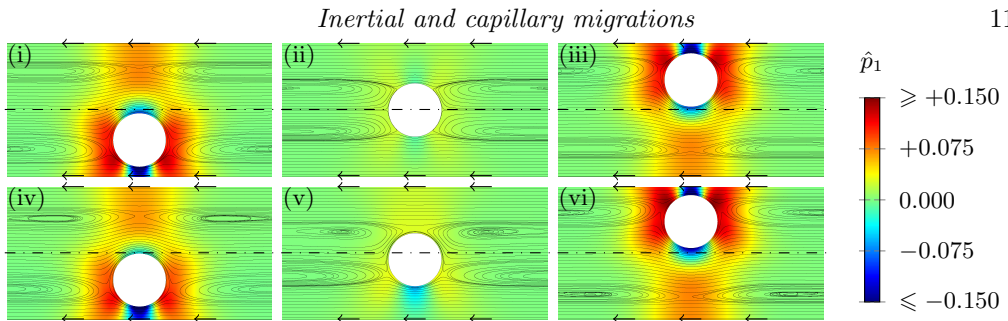


FIGURE 4. Streamlines of the creeping flow \mathbf{v}_0 and colormap for the pressure field of the pure linear inertial perturbation, \hat{p}_1 , at the symmetry plane $z = 0$ for (i-iii) neutral and (iv-vi) non-neutral $f/\text{Re}=-0.15$ bubbles with rigid interface and size $d = 0.4$. Labels corresponds to point solutions marked in fig. 2a.

The flow pattern and pressure field allows to rationalise expressions (3.9). In particular, the zeroth-order solutions, depicted in fig. 3, reveal the anti-symmetry and reversibility of the creeping flow. Therefore, the balanced body force vanishes, $f = 0$, as corroborated by the pressure field and the velocity of the bubble, the pressure drop and the rotational velocity are non-zero in general as it can be inferred from the anti-symmetry/reversibility of the flow. The positions of the bubbles in fig. 3 correspond to the points in fig. 2 labeled with the same roman number than the picture. Observe that points (i) and (iii) correspond to upside down flip due to the symmetry around the plane $y = 0$.

The behaviour of inertial migration can be explained with the help of the flow pattern and the pressure field of the first-order solution. In fig. 4, we depict the zeroth-order flow pattern and the first-order pressure field. In this case, the flow is symmetric and anti-reversible, as explained in app. B, which enforce the velocity, pressure drop and rotational velocity to vanish whereas non-zero balanced body force are allowed. In fig. 2a, points (i)-(iii) correspond to neutral bubbles which means that underpressure and overpressure zones should counterbalance each other, fig. 4i-iii. To understand their stability we plot in fig. 4iv-vi the counterpart for a moderate negative body force, as in fig. 2a. The displacement of bubbles from positions (i) and (iii) to (iv) and (vi), respectively, leads to a variation of the net force exerted on the bubble in the opposite direction to the displacement. It can be seen in both cases an increase of the underpressure and a decrease of the overpressure which provides the migration force balancing the body force. Contrarily, the displacement of (ii) to (iv) leads to a variation in this force in the same direction due to an underpressure from this side making this position unstable as inferred in fig. 2a.

In figs. 5 and 6, we plot the global variables f , V , β and Ω (if applicable) describing the bubble dynamics in the pure linear inertial regime, see table 1, as a function of the diameter and the position of the bubble (3.9). Because of numerical limitations, we only computed solutions within the ranges $0.1 \leq d \leq 0.9$ and $0 \leq \varepsilon \leq 0.95\varepsilon_*$.

In fig. 5, we depict the influence of the bubble size on the dynamics of bubbles with rigid interface (3.6). In fig. 5a, we plot the balanced body force f , related to the migration through the volume of the bubble by the dimensionless counterpart of (2.10). We observe that neutral bubbles, $f = 0$, with diameter smaller than $d \lesssim 0.73$ are unstable at the centred position, as revealed by the positive value of $\partial_\varepsilon f / \text{Re} > 0$. We also observe that centred bubbles with diameter $d \approx 0.3$ are the most unstable and that equilibrium positions get away from the centre as its size diminishes. The transition between unstable and stable position is depicted with black-dashed lines which corresponds to the extrema of fig. 2a, illustrated with ■ for $d = 0.4$. Some relevant conditions exhibiting these features

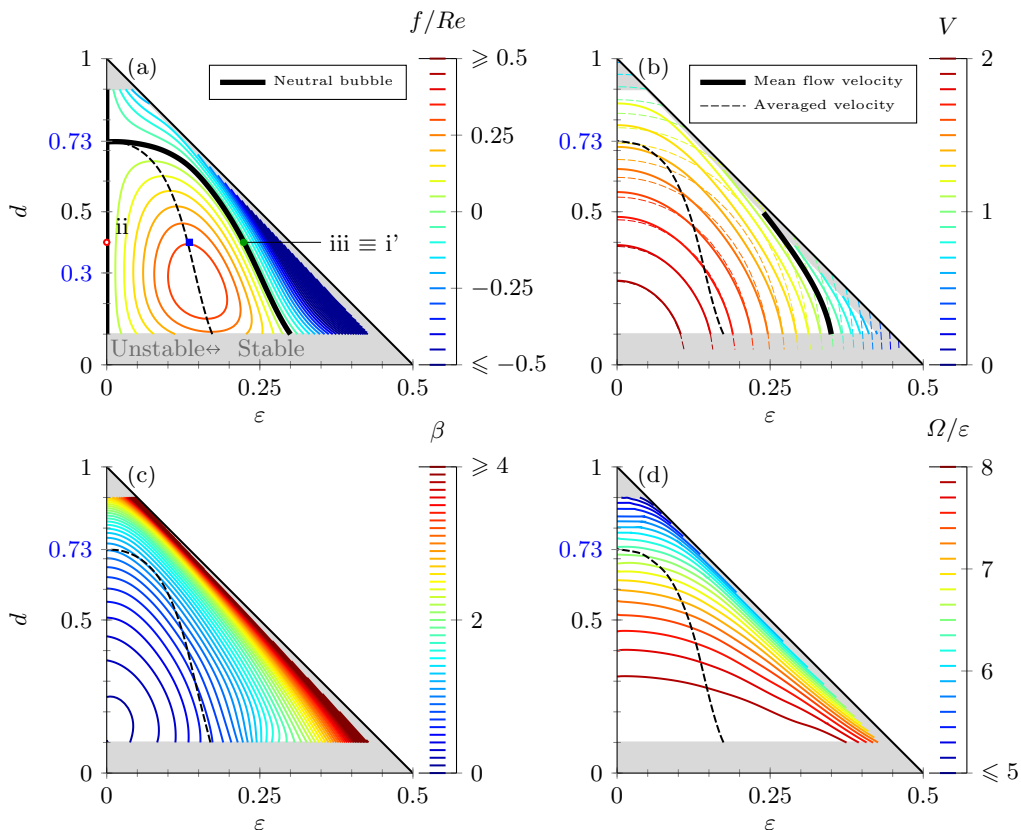


FIGURE 5. Effect of the eccentricity ε and the size d of bubbles with rigid interface in the pure linear inertial regime on the (a) balanced body force, (b) velocity of the bubble, (c) pressure correction factor and (d) rotational velocity of bubbles with rigid interface. \blacksquare Not explored, --- $\varepsilon = \varepsilon_*$ and - - - - stability transition.

are depicted in fig. 2a, see points (ii) and (iii) in fig. 2a. Small bubbles travel with the Poiseuille velocity and the rotational velocity of the bubble corresponds to the rotational velocity of the Poiseuille flow (half of the vorticity), $\Omega = -\frac{1}{2}\partial_\varepsilon 2[1 - 4\varepsilon^2] = 8\varepsilon$, as shown in fig. 5d. In fact, the bubble tends to assure continuity of the liquid at the rigid interface of the bubble with a velocity very similar to the average over the bubble surface of the Poiseuille velocity, $V \approx \Sigma_B^{-1} \int_{\Sigma_B} 2[1 - 4(y^2 + z^2)] d\Sigma$, as plotted in fig. 5b in coloured thin dashed lines. The rotational velocity, depicted in fig. 5d, also reduces due to the effect of the wall. Rigid bubbles behave like a plug since for large size the pressure drop increases with the bubble size as shown in fig. 5c.

In fig. 6, we depict the influence of the bubble size on the dynamics of the bubbles with stress-free interface (3.7). In fig. 6a, we plot the body force f , related to the migration force by the dimensionless counterpart of (2.10). Analogous behaviour to the rigid interface is observed. In this case the transition of stability for centred bubbles takes place at around $d \approx 0.85$ and the most unstable centred bubble are those with diameter $d \approx 0.63$. The range of position for which the bubble is unstable is larger than for rigid bubbles. We depict the equilibrium position of neutral bubbles illustrated by the points (ii) and (iii) in fig. 2a. We observe that it exists a range of bubble size for which bubbles are, in practice, touching the wall, $\varepsilon > 0.95\varepsilon_*$, as shown in fig. 1a. In fig. 6b, we can numerically observe that small bubbles follow the Poiseuille flow $V_P = 2(1 - 4\varepsilon^2)$ and,

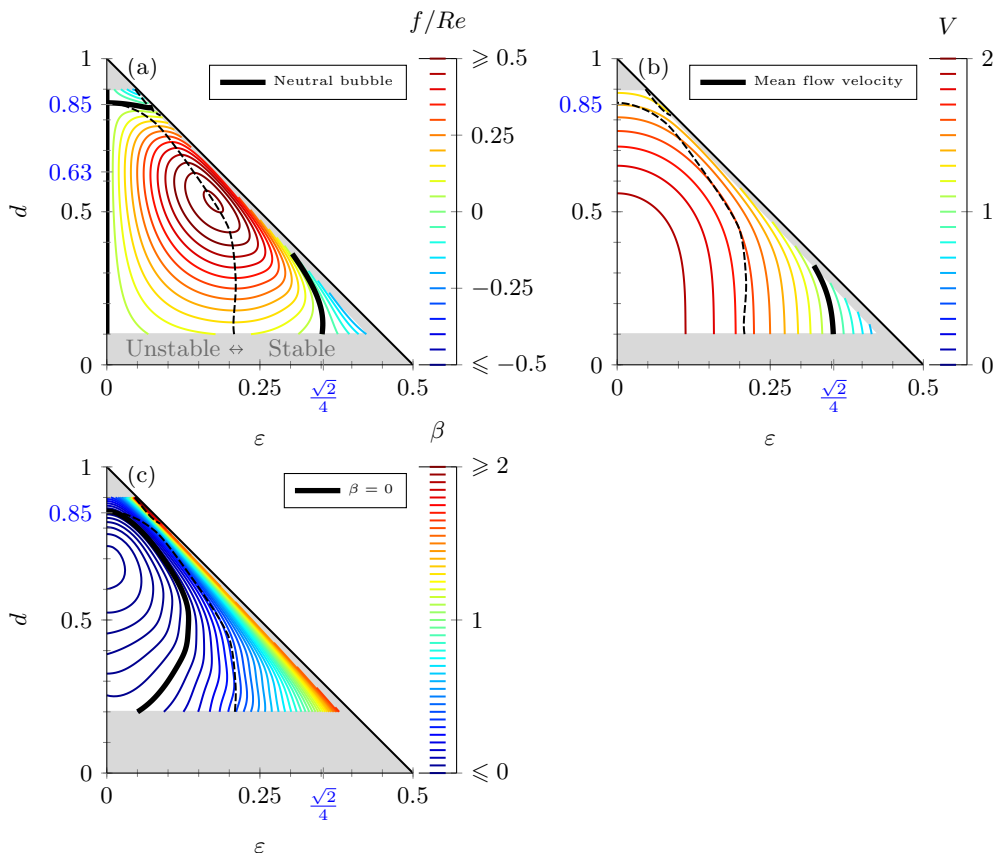


FIGURE 6. Effect of the eccentricity ε and the size d of bubbles with stress-free interface in the pure linear inertial regime on the (a) balanced body force, (b) velocity of the bubble and (c) pressure correction factor. \blacksquare Not explored, — $\varepsilon = \varepsilon_*$ and - - - stability transition.

in absence of body force, bubbles migrate to the position at which it travels at the mean flow, i.e. $V = V_P = 1$ at $\varepsilon = \sqrt{2}/4$. Proximity of the bubble to the wall, either because of bubble size or due to eccentricity, turns out to make the bubbles to travel slower. In fig. 6c, we observe the pressure correction factor due to the presence of the bubble. We highlight the conditions for which the pressure drop vanishes, which is the threshold of position of bubble size that reduces the pressure drop. Unfortunately, these positions are all unstable and stable bubbles in the pure linear inertial regime always increase the pressure drop.

We obtained the coefficients k_i 's of the asymptotic behaviour of the balanced body force for small bubble size $d \rightarrow 0$ for the pure linear inertial regime given the following expression

$$\frac{f(\varepsilon, d)}{Re} \approx \sum_{i=0}^N k_i(\varepsilon) d^i. \quad (3.10)$$

Since the range of feasible d for constant ε vanishes as $\varepsilon \rightarrow \varepsilon_*$, it is numerically convenient to rather obtain the expansion $f(\varepsilon/\varepsilon_*, d)/Re \approx \sum_{i=0}^N c_i(\varepsilon/\varepsilon_*) d^i$ whose coefficients c_i 's can be related to those in (3.10) by its Taylor's expansion around $d = 0$. In effect, $\hat{k}_i(\varepsilon/\varepsilon_*) \approx \hat{k}_i(2\varepsilon) - 2\varepsilon d \partial_{\varepsilon/\varepsilon_*} \hat{k}_i|_{\varepsilon/\varepsilon_* = 2\varepsilon} + \dots$, where the limit $\lim_{d \rightarrow 0} \varepsilon/\varepsilon_* = 2\varepsilon$ has been

| | | | | | | | | |
|-------------|-----------|----------------------|-----|------------------------|-----|------------------------|-----|------------------------|
| Rigid | $k_1 = +$ | $15.0(2\varepsilon)$ | $-$ | $34.1(2\varepsilon)^3$ | $-$ | $10.5(2\varepsilon)^5$ | $+$ | $8.9(2\varepsilon)^7$ |
| | $k_2 = -$ | $93(2\varepsilon)$ | $+$ | $332(2\varepsilon)^3$ | $+$ | $276(2\varepsilon)^5$ | $-$ | $264(2\varepsilon)^7$ |
| Stress-free | $k_1 = +$ | $3.11(2\varepsilon)$ | $-$ | $5.66(2\varepsilon)^3$ | $-$ | $2.89(2\varepsilon)^5$ | $-$ | $0.61(2\varepsilon)^7$ |
| | $k_2 = -$ | $1.4(2\varepsilon)$ | $+$ | $29.1(2\varepsilon)^3$ | $+$ | $70.0(2\varepsilon)^5$ | $+$ | $10.1(2\varepsilon)^7$ |

TABLE 2. Polynomial fitting of the behaviour of the balanced body force in the small size limit $d \rightarrow 0$ in the pure linear inertial regime (3.10). Note that $k_0 = 0$ (see text for details).

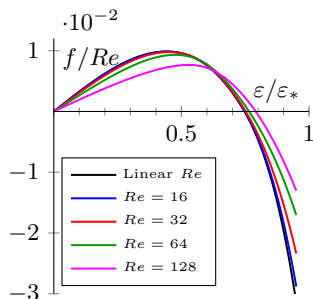


FIGURE 7. The influence of the Re number on the balanced body force for bubbles of size $d = 0.4$ with rigid interface in the pure nonlinear inertial regime.

taken into account. We took values of $N = 2$ and $0.1 < d < 0.2$ that ensures independency of the results on the particular choice. With this procedure, we obtained the polynomial expansion (3.10) given in table 2 where the zeroth-term k_0 has been found to vanish as predicted by Hood *et al.* (2015) for the rigid case. Observe the first term represents the asymptotic behaviour obtained by Ho & Leal (1974) and the second term is a correction also considered by Hood *et al.* (2015).

For sufficiently large Re numbers, the solution (3.9) is no longer valid as we observe in fig. 7, where the balanced body force is depicted versus the eccentricity for various Reynolds numbers for a bubble with diameter $d = 0.4$ in the case of rigid interface bubbles and pure nonlinear inertial regime. Anyhow, the behaviour remains qualitatively similar to the pure linear inertial migration.

The validity of the pure linear inertial flow, $Re < Re_*$, can be quantified as follows with two different criteria depicted in fig. 8. On the one hand, in fig. 8a,c, we plot the influence of the Reynolds number and the bubble size on the stability of the centred position given by $\partial_\varepsilon f/Re|_{\varepsilon=0}$. It can be observed that the range of validity of small Re is slightly larger for stress-free bubbles than with rigid interface and both limits are around, $Re < Re_* \approx 32$ as far as stable positions are concerned. Note that this limit is not valid in the vicinity of 0.3 and 0.63, respectively, but it only concerns unstable positions. On the other hand, the equilibrium position of neutral bubbles is modified. In fig. 8b,d, we plot the influence of the Re number on the equilibrium position of a bubble of certain size in absence of body force, and we observe that this position varies for $Re > 32$ for small bubbles and for $Re > 64$ for large bubbles, therefore, the criteria $Re_* \approx 32$ is also valid in both cases. The nonlinear effect of the inertia turns out to be destabilising, in general, whether regarding the stability of the equilibrium or the neutral bubble position.

3.2. Capillary migration.

Migration forces may also arise if the bubbles are deformable. In this case, the reversibility of the creeping flow is broken due to the anti-symmetric deformation of the

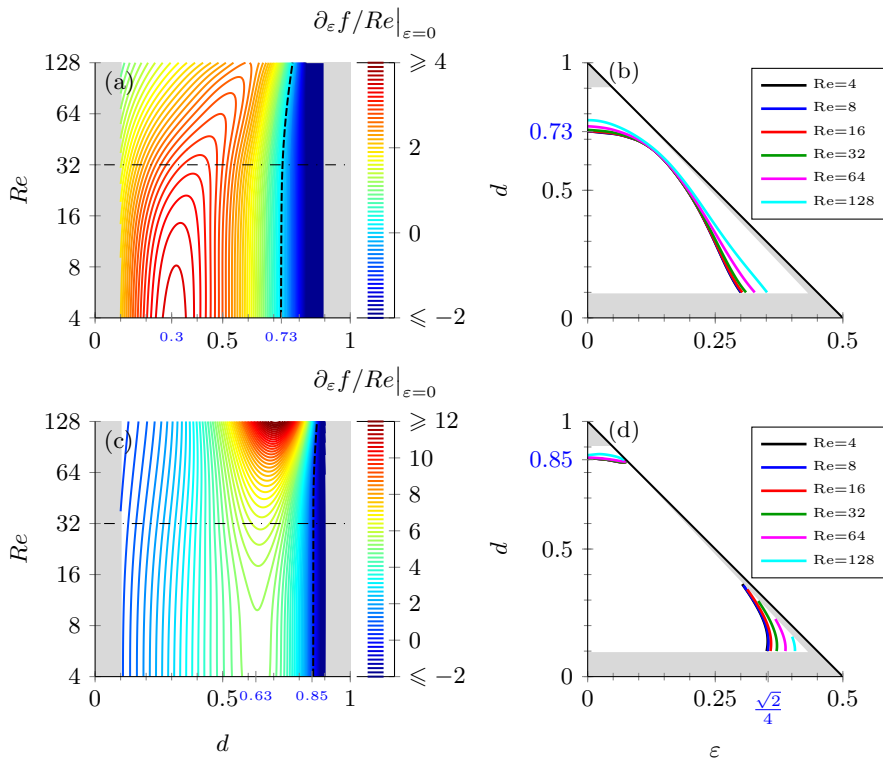


FIGURE 8. Influence of the Re number and the size of bubbles with (a-b) rigid or (c-d) stress-free interfaces in pure nonlinear inertial flow for bubbles on the (a,c) slope of the balanced migration force exerted on centred bubbles with respect to eccentricity (---- stability transition) and (b,d) on the equilibrium position of neutral bubbles. \blacksquare Not explored and validity criteria \cdots $Re < Re_*(d)$.

bubble. Indeed, the bubble deforms differently in its front and rear side, due to pressure gradients of the creeping flow along the surface of the bubble. In fig. 9, the deformation of the bubble due to the viscous and pressure forces exerted on its surface in the pure nonlinear capillary regime is depicted for a given values of the eccentricity and bubble size whereas the Ca is varied. In particular, it can be observed that the overpressure (underpressure) for small Ca numbers (which tends to the case of stress-free bubbles in the leading order creeping flow regime as $Ca \rightarrow 0$) shown in fig. 9a corresponds to a decrease (increase) of surface curvature and the bubble deforms as shown in fig. 9b-c for larger deformability of the bubble, i.e. larger Ca numbers. The capillary migration force exerted on the bubble surface always points towards the centre of the channel as inferred from the dominant effect of the overpressure in fig. 9b-c.

The analogous role of the Ca numbers in the pure capillary regime, as compared to the Re number in the pure inertial regime, motivates an expansion of the system of equations (2.1)-(2.2), (2.4)-(2.5), (2.9)-(2.12) as $\psi = \sum_{j=0}^{\infty} Ca^j \psi_j$, where ψ represents any of the dependent variables \hat{p} , \mathbf{v} , f , $p_G - 4/(dCa)$, δ/Ca , V or Δp where the normal displacement of the bubble surface δ is additionally considered.

Then, the expanded Navier-Stokes equations with neglecting inertia, $Re = 0$, become

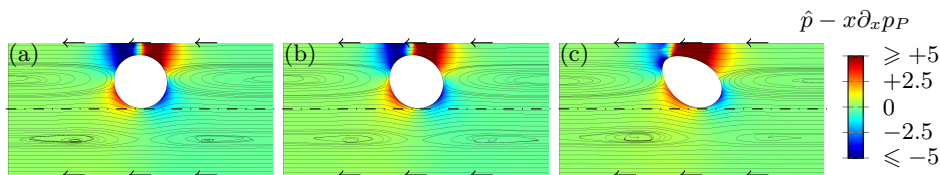


FIGURE 9. Streamlines of the pure nonlinear capillary flow, \mathbf{v} , and colormap for the pressure field, $\hat{p} - x\partial_x p_P$, of the pure nonlinear capillary flow at the symmetry plane with bubble size $d = 0.4$ centred at $\varepsilon = 0.7\varepsilon_*$ and capillary numbers (a) $Ca = 1/64$, (b) $Ca = 1/16$ and (c) $Ca = 1/4$.

$$\nabla \cdot \mathbf{v}_0 = 0, \quad \mathbf{0} = -\nabla \hat{p}_0 + \nabla \cdot \boldsymbol{\tau}_0 \quad \text{at } \mathcal{V}_0, \quad (3.11a)$$

$$\nabla \cdot \mathbf{v}_1 = 0, \quad \mathbf{0} = -\nabla \hat{p}_1 + \nabla \cdot \boldsymbol{\tau}_1 \quad \text{at } \mathcal{V}_0, \quad (3.11b)$$

which must be solved at the undeformed domain, \mathcal{V}_0 , and together with the boundary conditions at the wall (3.2) and the pseudo-periodic conditions (3.4) to accommodate the flow rate (3.5). In addition, the boundary conditions on the bubble surface (2.11) has to be perturbed and the zeroth order yields

$$\mathbf{n} \cdot \{[-\hat{p}_0 - \mathbf{f}_0 \cdot (\mathbf{x} - \boldsymbol{\varepsilon}) + p_{G0}] \mathcal{I} + \boldsymbol{\tau}_0\} = (\hat{\nabla}_S \cdot \nabla_S \delta_0 - \frac{8\delta_0}{d^2}) \mathbf{n} \quad \text{at } \Sigma_{B_0}, \quad (3.12a)$$

$$\mathbf{v}_0 \cdot \mathbf{n} = 0 \quad \text{at } \Sigma_{B_0} \quad (3.12b)$$

whereas the first order writes

$$\mathbf{n} \cdot \{[-\hat{p}_1 - \mathbf{f}_1 \cdot (\mathbf{x} - \boldsymbol{\varepsilon}) + p_{G1}] \mathcal{I} + \boldsymbol{\tau}_1\} +$$

$$+\hat{\nabla}_S \cdot \delta_0 \{[-\hat{p}_0 - \mathbf{f}_0 \cdot (\mathbf{x} - \boldsymbol{\varepsilon}) + p_{G0}] \mathcal{I} + \boldsymbol{\tau}_0\} = (\hat{\nabla}_S \cdot \nabla_S \delta_1 - \frac{8\delta_1}{d^2}) \mathbf{n} \quad \text{at } \Sigma_{B_0}, \quad (3.13a)$$

$$\mathbf{v}_1 \cdot \mathbf{n} + \hat{\nabla}_S \cdot \delta_0 \mathbf{v}_0 = 0 \quad \text{at } \Sigma_{B_0}, \quad (3.13b)$$

where Σ_{B_0} is the undeformed surface of the bubble, on which the surface operator $\nabla_S \varphi = \mathcal{I}_S \cdot \nabla \varphi$ is defined. The method used to obtain the linearisation (3.13) is given in app. A. The perturbation of the position and volume restriction (2.12) writes

$$\int_{\Sigma_{B_0}} \delta_0 \, d\Sigma = 0, \quad \int_{\Sigma_{B_0}} \delta_1 \, d\Sigma = 0, \quad (3.14a)$$

$$\int_{\Sigma_{B_0}} \delta_0 \mathbf{n} \, d\Sigma = \mathbf{0}, \quad \int_{\Sigma_{B_0}} \delta_1 \mathbf{n} \, d\Sigma = \mathbf{0}. \quad (3.14b)$$

Solutions of this system for the balanced body force, velocity of the bubble and pressure correction factor are of the form

$$f_\gamma \equiv f/Ca \approx f_1(\varepsilon, d), \quad V \approx V_0(\varepsilon, d), \quad \beta \approx \beta_0(\varepsilon, d), \quad (3.15)$$

where the removed terms have been found numerically to be vanishing, i.e. $f_0 = V_1 = \beta_1 = 0$ as it can be inferred from the symmetries and reversibilities of the flow. Observe that the capillary migration force comes from the first-order solution whereas the velocity, pressure drop and the rotation come up from the creeping flow, analogous to the inertial migration case.

In fig. 10, we depict solutions of the pure nonlinear capillary flow for several Ca numbers and its linear limit to which nonlinear converges when the Ca is sufficiently small $Ca < Ca_*$, see table 1. The dependence of the balanced body force, the velocity and the pressure

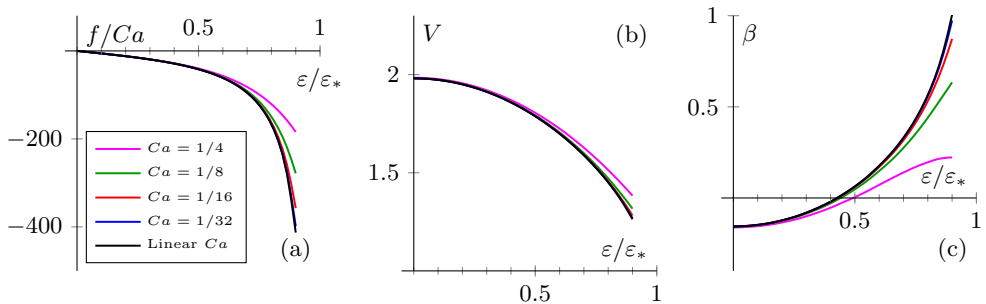


FIGURE 10. Effect of the deformability of bubbles with size $d = 0.4$ and the eccentricity in the pure nonlinear capillary regime on the (a) balanced body force, (b) velocity of the bubble and (c) pressure correction factor.

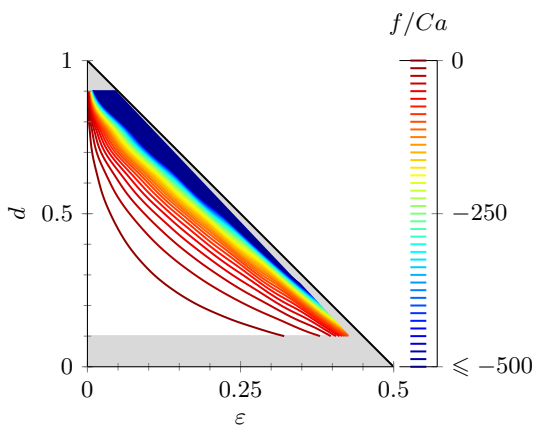


FIGURE 11. Effect of the eccentricity ε and the size d of bubbles in the pure linear capillary regime on the balanced body force. \blacksquare Not explored and — $\varepsilon = \varepsilon_*$.

drop on the eccentricity is shown for a given bubble size. Observe that the capillary migration force yields to only stable equilibrium positions, since $\partial_\varepsilon f < 0$ as shown in fig. 10a. We also observe that large deformations reduce bubble migration, increase the velocity of the bubbles and reduces the associated pressure drop. In fig. 10b and c, the limit of pure linear capillary regime reproduces the velocity of the bubble and the pressure drop for stress-free bubbles in the leading order creeping flow, V_0 and Δp_0 , being the latter negative for some conditions. However in this case, the bubble is stable for these conditions and, therefore, the presence of deformable bubbles may reduce the pressure drop.

The balanced body force in the pure linear capillary regime is depicted in fig. 11. Bubbles experience a stronger repulsion from the wall as they become closer to it either because of their size or because of their position. For the velocity and pressure correction factor, same results than for the inertial migration of bubbles with stress-free surfaces is encountered, see fig. 6b-c. The balanced body force experienced by small bubbles in the pure capillary migration regime is analogous to that of the inertial case (3.10) and writes

$$\frac{f(\varepsilon, d)}{Ca} \approx \sum_{i=0}^N k_i(\varepsilon) d^i, \quad (3.16)$$

| | |
|------------|---|
| Deformable | $k_1 = -110(2\varepsilon) + 79(2\varepsilon)^3 - 235(2\varepsilon)^5 + 52(2\varepsilon)^7$ |
| | $k_2 = +136(2\varepsilon) - 257(2\varepsilon)^3 - 1819(2\varepsilon)^5 + 824(2\varepsilon)^7$ |

TABLE 3. Polynomial fitting of the behaviour of the balanced body force in the small size limit $d \rightarrow 0$ in the pure linear capillary regime (3.16). Note that $k_0 = 0$ (see text for details).

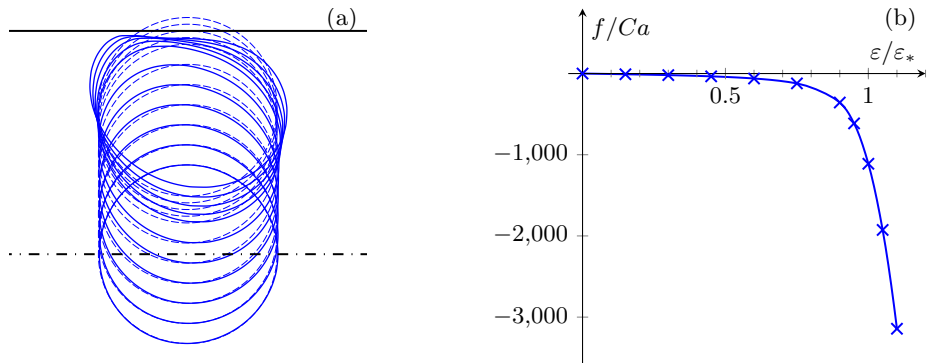


FIGURE 12. Effect of the eccentricity (a) on the shape of bubbles at the symmetry plane $z = 0$ and (b) on the balanced body force in the pure nonlinear capillary regime with $Ca = 1/16$ for bubbles with size $d = 0.4$. ---- Undeformed shape, — deformed shape and \times discrete values of $\varepsilon/\varepsilon_*$ plotted in (a).

which is obtained in the same manner than (3.10). In the pure linear capillary migration regime the constants are given in table 3. The coefficient k_0 has been found to vanish as predicted by Chan & Leal (1979).

The validity of the pure linear capillary regime is lost either for not sufficiently small capillary numbers, see fig. 10a, leading to large deformation all around the bubble, or for smaller capillary numbers if the gap between the bubble and the wall is small, leading to an increase of the local stresses, and, therefore, larger deformation in this region whereas the rest of the bubble remains mainly spherical. The latter effect is shown in fig. 12, where the behaviour of a bubble with $Ca = 1/20$ is depicted. In fig. 12a, the bubble contour at the symmetry plane is plotted at different positions. The bubble remains almost spherical until the wall effect is noticeable for positions at which a liquid layer prevent the bubble to touch the wall by deforming and drastically peeling it from the wall, see fig. 12b. Observe, that since the bubble deforms, the centre of the bubble can get closer to the wall and hence its feasible range is $-0.5 < \varepsilon < 0.5$ instead of the corresponding to undeformable bubbles $-\varepsilon_* < \varepsilon < \varepsilon_*$. However, in these additional regions, $\varepsilon < -\varepsilon_*$ and $\varepsilon > \varepsilon_*$, nonlinear effects are always present and the linear regime is not only nonsense but numerically impossible. The effect of the deformability on the velocity and the pressure drop are not qualitatively different than in fig. 10, hence not shown.

Now, it remains to explore the validity of the pure linear capillary regime. On the one hand, we avoid nonlinear effect due to the proximity of the wall and study centred bubbles. We depict the stability measurement of the centred positions, $\partial_\varepsilon f/Ca|_{\varepsilon=0}$ and observe in fig. 13a that the validity range strongly depends on the bubble size, in particular the stability increases with the bubble size but the validity of the pure linear capillary flow reduces as $\log_2 Ca_* \approx 1 - 7d$. We also depict the velocity of the bubble and observe that bubbles travel faster when they are strongly deformed, and may

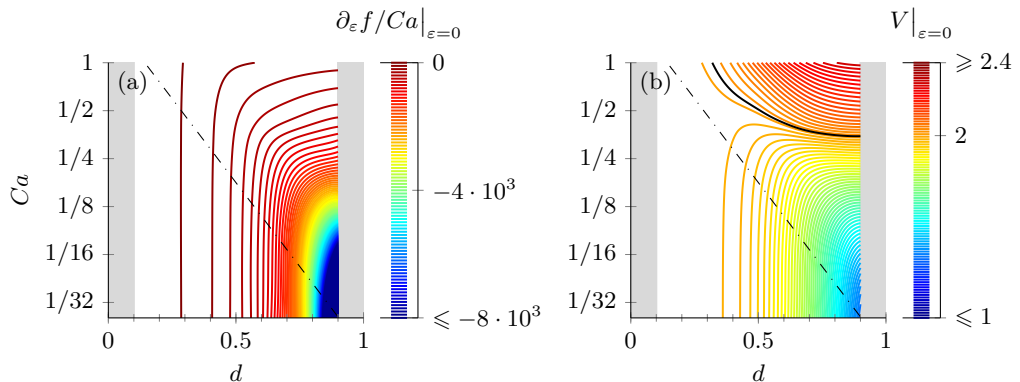


FIGURE 13. Influence of the Ca number and the size of the bubble in pure nonlinear capillary regime on the (a) slope of the balanced migration force exerted on centred bubbles with respect to eccentricity ($\varepsilon = 0$) and (b) on the velocity of centred bubbles, — $V = 2$. Not explored and validity criteria $\cdots \cdots Ca < Ca_*(d) \approx 2^{1-7d}$.

eventually travels faster than the maximum velocity of the liquid - twice the mean flow. We carefully checked it is not a numerical artefact of the simulations.

On the other hand, we study the nonlinearities due to the proximity of the wall and the bubble is locally deformed by the presence of the wall (fig. 14b). In fig. 14, we depict the behaviour of the bubble at $\varepsilon = \varepsilon_*$ where the nonlinearities due to the proximity of the wall are dominant. The gap between the bubble and the wall follows the Landau-Levich $2/3$ power law at least for sufficiently small Ca as shown in fig. 14a contrarily to centred bubbles. The balanced body force is not proportional to the Ca number and the pure linear capillary regime is not valid (fig. 14b), deformed bubbles travel faster (fig. 14c) and the pressure drop decreases and can even take negative values (fig. 14d).

3.3. Inertial versus capillary migration

We study the equilibrium position of bubbles when inertial and capillary migration are taken into account as a function of the Re and Ca numbers and the size of the bubble d in the linear regime. If we focus on neutral bubbles, the balanced body force $f \approx Re f_\rho + Ca f_\gamma$ must vanish and then, the equilibrium position depends on the Ohnesorge number, $Oh^2 = Ca/Re$, instead of the Re and Ca numbers separately. In fig. 15 we plot the uncentered and stable equilibrium position of neutral bubbles for given Oh number. We observe that as $Oh \rightarrow 0$, the equilibrium positions tend to that of the pure linear inertial regime. Contrarily, if the Oh number become larger, the uncentered equilibrium position tends get closer to the centre of the channel and eventually vanishes for sufficiently large values, as in the pure linear capillary regime. Observe that also centred positions exists but they are not depicted for the sake of clarity.

Next, we study the stability of the centred position as a function of the Oh number and the size of the bubble d . In the linear inertial-capillary regime, the stability is governed by the sign of $\partial_\varepsilon(Re f_\rho + Ca f_\gamma)$ and therefore the dependence on the Re and Ca numbers is through the Oh number. In fig. 16a, we plot the stability map as a function of the bubble size d and the Oh number in the linear regime. We observe that there exist both threshold on the Oh number and bubble size above which the centred position is always stable. Observe that this curve is also given in fig. 15, since the transition between stable and unstable centred positions occurs where the branch of stable uncentered positions appears similar to the behaviour of neutral bubbles in the pure linear migration regime,

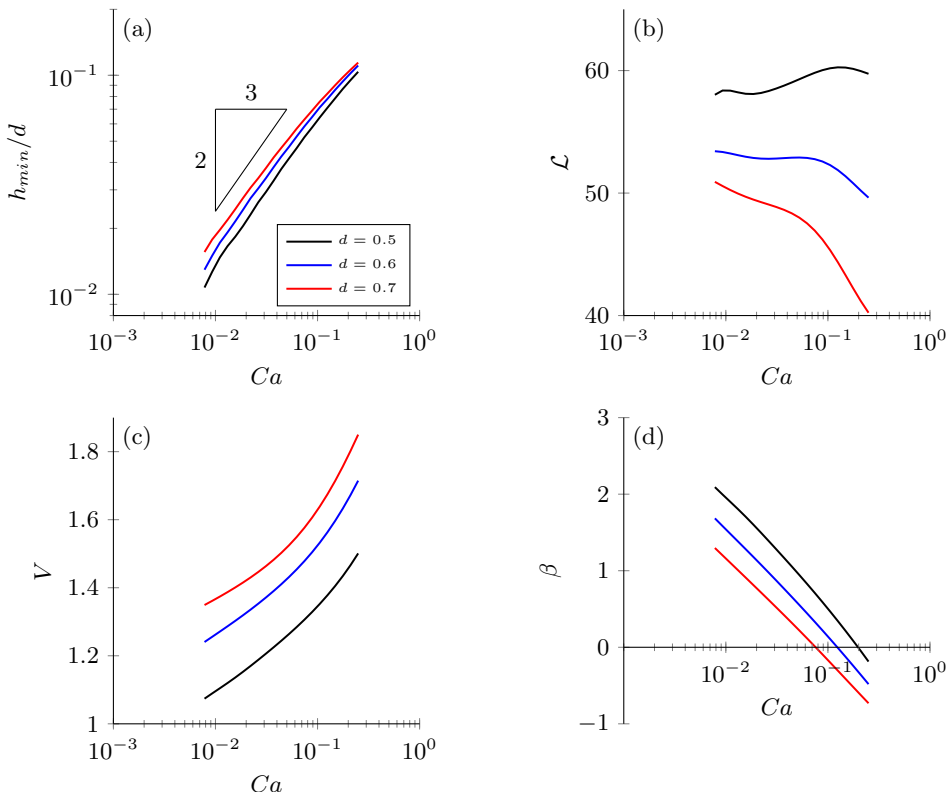


FIGURE 14. Influence of the Ca number in the pure nonlinear capillary regime for bubbles centred at $\varepsilon = \varepsilon_*$, where nonlinearities due to the proximity of the wall are dominant, on (a) the minimum gap between the wall and the bubble, (b) the balanced body force, (c) the velocity and (d) the pressure correction factor.

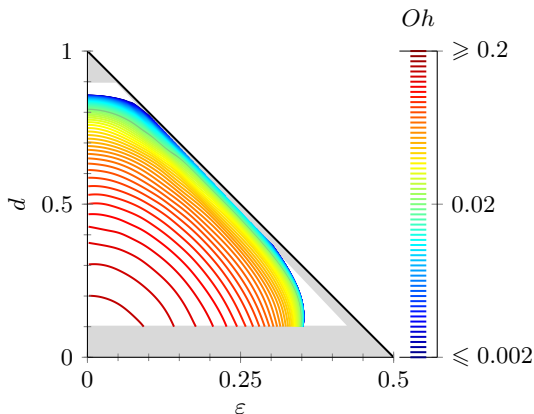


FIGURE 15. Influence of the Oh number and the bubble size d on the equilibrium position of neutral bubbles, $f = 0$, in the linear inertial-capillary regime. \blacksquare Not explored and --- $\varepsilon = \varepsilon_*$.

see fig. 5 or 6. In fig. 16b, we depict the stability map for several bubble sizes on the Re - Ca plane in the nonlinear inertial-capillary regime, and therefore, considering interactions between inertial and capillary migration as well as the effects out of the linear inertial-capillary regime. The linear inertial-capillary regime is recovered for $Re < Re_* \approx 8$,

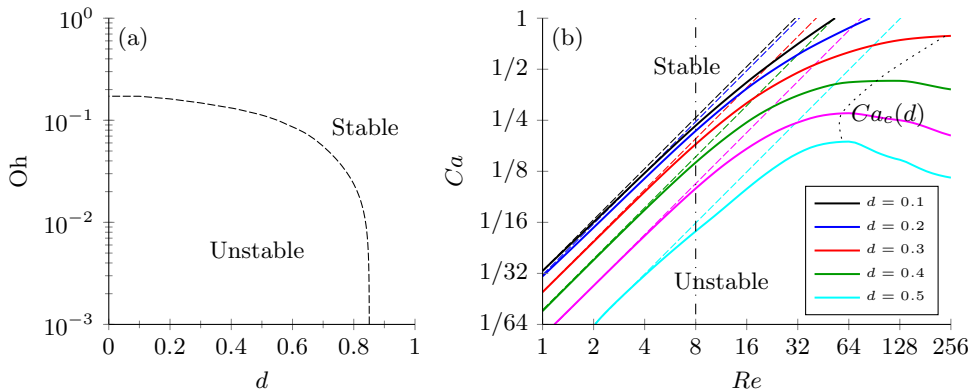


FIGURE 16. Stability diagram for centred bubbles in ---- the linear and nonlinear — inertial-capillary regime. (a) Effect of the bubble size and Oh number in the linear regime and (b) nonlinear joint effect of inertia and deformability of the bubble. --- Validity of the linear regime $Re < Re_* \approx 8$ and $\forall Ca$.

whereas the nonlinear effects are strongly stabilising above the threshold $Re > Re_* \approx 8$ which is reduced from 32 due to the joint effect with capillary deformation. In particular, there exist for each bubble size, a value of the Ca number depending on the bubble size $Ca_c(d)$ above which centred bubbles are always stable, regardless the value of the Re number, i.e. the destabilising effect of inertia is overcome by the stabilising effect of the additional deformation of the bubble interface due to the effect of the inertia. On the contrary, for values of the Ca number smaller than Ca_c , a range of Re numbers is found for which bubbles are unstable.

4. Conclusions and discussion

This paper reports the dynamics of a train of bubbles regarding the flow structure and the migration forces with both an inertial and capillary deformation origin. We write the general equations governing the dynamics of a train of bubbles. We assume the change of size of the bubble along the channel to be slow compared to the characteristic hydrodynamic time and that no turbulence develops. Under these assumptions, the flow can be considered quasi-stationary and time dependence can be dropped out. We quantitatively studied the influence of the bubble size and of body force on the linear inertial and capillary regimes. To do this, regular asymptotic expansions of the governing equations are carried out, including the linearisation of the boundary conditions of the deformable surface of the bubble around the undeformed shape -for which we provide a new asymptotical approach. Then, we compare with the nonlinear regimes governed by the full system of equations in order to obtain the validity of the linear regimes for the Re and Ca numbers.

In the case of inertial migration, we report the well-known multiple equilibrium behaviour and we illustrate the underlying hydrodynamics mechanism regarding at the first-order pressure field correction of the creeping flow. Then, we describe the influence of the bubble size and the eccentricity of the equilibrium positions on the external uniform body force that balances the migration force, the velocity of the bubble, the additional pressure drop (pressure correction factor) due to the presence of the bubble and the rotational velocity (only applicable in the case of rigid interface bubbles). Since external body force is commonly given, first, the position of the bubble has to be obtained to ensure the transverse equilibrium. Once the equilibrium position is obtained, the velocity,

additional pressure drop and rotation of the bubble (if applicable) can be obtained. In agreement with previous results, small bubbles follows the Poiseuille flow and neutral bubbles (in absence of body force) migrates to the position at which the Poiseuille flow and the mean flow coincide, i.e. at $\varepsilon = \sqrt{2}/4$ in the case of stress-free bubbles. We also observe that the surface average of the Poiseuille velocity provides a reasonably good approximation of the bubble velocity for rigid surfaces. We observe that stress-free neutral bubbles with a size smaller than $d < 0.83$ migrates out of the centre and within the range $0.35 < d < 0.84$ migrates to the wall, i.e. to $\varepsilon > 0.95\varepsilon_*$ where $\varepsilon_* = \frac{1}{2}(1 - d)$. Bubbles with rigid interface and with size smaller than $d < 0.73$ migrate to intermediate positions. We also observed that the presence of the bubbles may reduce the pressure drop along the channel. However, this region is unstable due to inertial migration forces but may be stabilised by capillary migration force. A plug effect is observed for rigid particles that dramatically increases the pressure drop with the bubble size. Small rigid particles tends to rotate with the same rotational velocity than the Poiseuille flow as the bubble size decreases. After, we studied the validity of the linear inertial regime and obtained a criteria based on the stability of the centred position and the equilibrium position of neutral bubbles. In both rigid and stress-free cases nonlinearities break the validity of the linear regime for Re numbers larger than the threshold $Re_* \approx 32$ as well as shift the equilibrium positions toward the wall. Also, polynomial fitting is obtained for the limit predicted by Hood *et al.* (2015) for small bubbles $d \rightarrow 0$.

On the other hand, we considered the behaviour of deformable bubbles. In this case, underpressure and overpressure of the creeping flow on the bubble surface make it deform leading to stabilising forces pointing towards the centre of the channel. We obtained the regular asymptotic expansion of the governing equations for small values of the Ca number. Since the boundaries of the domain at the bubble surface deforms, it is necessary to linearise around the undeformed shape the boundary condition applied at this boundary. We observed that larger bubbles balance larger outer forces at the same equilibrium position and its effect dramatically increases as the bubble approaches the wall due to either larger bubble size or eccentricity. Polynomial fitting is obtained for the limit of small bubbles $d \rightarrow 0$. The linear capillary limit is valid for centred bubbles if the Ca number is smaller than the threshold $\log_2 Ca_* \approx 2 - 7d$ which decreases with the eccentricity until it is no longer valid for undeformed bubbles touching the wall. In this case, a thin lubrication layer forms between the wall and the bubble due to the deformation of the later. The film thickness follows the $2/3$ Landau-Levich power law for $Ca < 0.1$, the migration force very slightly depends on the surface tension (no longer proportional to the Ca number) and the velocity of the bubble increases with its deformation while the pressure drop decreases and can even reach negative values.

Finally, we obtain the transverse equilibrium position of neutral bubbles and the stability of the centred position (for neutral bubbles) taking into account both inertia and deformability. We obtain a stability diagram depending on the $Oh = \sqrt{Ca/Re}$ number and the bubble size in the pure linear inertial-capillary regimes. We observed that centred solution are stable for either Oh numbers larger than $Oh > 0.2$ or for bubbles larger than $d < 0.85$, with a smooth transition between both limits. We also observe that the nonlinear effects are no longer negligible for Re numbers larger than $Re_* \approx 8$ above which nonlinear inertial-capillary effects becomes stabilizing even for given Ca number, contrarily as it happens in the pure nonlinear inertial regime.

The dynamics of drops in microchannels are of great interest in the scientific community and this work implicitly explore the limiting cases of very high/low viscosity drops. In particular, on the one hand the case of low viscosity drops exhibit the same behaviour of capillary deformable bubbles with stress-free bubbles for both inertial and capillary

(deformation-induced) migration. On the other hand, the case of high viscosity exhibits the same behaviour of the rigid interface and no deformation-induced migration takes place because deformation is prevented to occur. However, the transition of the dynamics for the viscosity of the drop, i.e. for intermediate viscosities, is still to be systematically studied.

We also provide an approach for the linearisation of the boundary conditions around the equilibrium position of a deformable boundary which rely on surface differential equations. This approach provides a powerful and simple theoretical background for other applications relying on deformable boundaries in complex geometries, such as global stability analysis of free interfaces in the most general conditions.

Acknowledgements

We thank the Brussels region for the financial support of this project through the WBGreen-MicroEco project. B.S. thanks the F.R.S.-FNRS for financial support as well as the IAP-7/38 MicroMAST project for supporting this research. This work was also performed under the umbrella of COST Action MP1106. We thank Benoit Haut, David Mikaelian and Miguel Pérez-Saborid for useful discussions.

Appendix A. Boundary conditions linearisation

Let $u(\mathbf{x})$ be a scalar, vectorial or tensor quantity defined on a deformable domain \mathcal{V} with boundary Σ and governed by Laplace equation

$$\nabla^2 u = 0 \quad \text{at } \mathcal{V}, \quad (\text{A } 1)$$

subject to Robin boundary conditions

$$\alpha u + \beta \mathbf{n} \cdot \nabla u = \gamma(\mathbf{x}) \quad \text{at } \Sigma, \quad (\text{A } 2)$$

where the deformation of the domain is given for the sake of simplicity and without loss of generality.

Considering an expansion of the variable u around a deformable domain, \mathcal{V}_0 , whose boundary experiences a displacement $\varepsilon \delta \mathbf{n}$, where $\varepsilon \ll 1$ is arbitrarily small,

$$u(\mathbf{x}) \approx u_0(\mathbf{x}) + \varepsilon u_1(\mathbf{x}) \quad \text{at } \mathcal{V}_0, \quad (\text{A } 3)$$

the linearisation of (A 1), substituting (A 3), gives

$$\nabla^2 u_0 = 0 \quad \text{and} \quad \nabla^2 u_1 = 0 \quad \text{at } \mathcal{V}_0. \quad (\text{A } 4)$$

The Dirichlet and non-homogeneous terms in (A 2) can be linearised as

$$u(\mathbf{x} + \varepsilon \delta \mathbf{n}_0) \approx u(\mathbf{x}) + \varepsilon \delta \mathbf{n}_0 \cdot \nabla u(\mathbf{x}) \quad \text{at } \partial \mathcal{V}_0, \quad (\text{A } 5a)$$

$$\gamma(\mathbf{x} + \varepsilon \delta \mathbf{n}_0) \approx \gamma(\mathbf{x}) + \varepsilon \delta \mathbf{n}_0 \cdot \nabla \gamma(\mathbf{x}) \quad \text{at } \partial \mathcal{V}_0, \quad (\text{A } 5b)$$

where \mathbf{n}_0 is the outer normal of the surface $\partial \mathcal{V}_0$. The Neumann term requires also linearisation of the normal vector,

$$\mathbf{n}(\mathbf{x} + \varepsilon \delta \mathbf{n}_0) \approx \mathbf{n}_0(\mathbf{x}) + \varepsilon \mathbf{n}_1(\mathbf{x}) \quad \text{at } \partial \mathcal{V}_0, \quad (\text{A } 6)$$

and can be written as

$$\mathbf{n}(\mathbf{x} + \varepsilon \delta \mathbf{n}_0) \cdot \nabla u(\mathbf{x} + \varepsilon \delta \mathbf{n}_0) \approx \mathbf{n}_0 \cdot \nabla u(\mathbf{x}) + \varepsilon \{ \mathbf{n}_1 \cdot \nabla u(\mathbf{x}) + \mathbf{n}_0 \cdot \nabla [\delta \mathbf{n}_0 \cdot \nabla u(\mathbf{x})] \} \quad \text{at } \partial \mathcal{V}_0 \quad (\text{A } 7)$$

Nevertheless, the evaluation of (A 7) involve tedious algebra which dramatically increases for PDE governing vectorial fields and a method to relate \mathbf{n}_1 with the surface displacement is needed. For these reasons, we propose an alternative approach which circumvents these drawbacks. It relies on the definition of surface operators acting on any scalar, vectorial or tensor quantity φ

$$\nabla_S \varphi = \mathcal{I}_S \cdot \nabla \varphi \quad \text{at } \partial \mathcal{V}_0, \quad (\text{A } 8a)$$

$$\hat{\nabla}_S \varphi = \nabla \cdot (\mathcal{I}_S \varphi) \quad \text{at } \partial \mathcal{V}_0, \quad (\text{A } 8b)$$

which represent surface and intrinsic surface gradients, respectively.

Let \mathcal{V}_1 be the volume generated by the normal displacement $\varepsilon \delta \mathbf{n}_0$ of a differential surface $d\Sigma_0$ on the boundary of \mathcal{V}_0 into $d\Sigma_1$. Then, the integral of (A 1) over this volume divided by the differential surface writes using the divergence theorem, in terms of the surface integral over the surface $d\Sigma_0$, over its displaced counterpart $d\Sigma_1$ and over the generatrix of the volume \mathcal{V}_1 , as

$$\lim_{d\Sigma_0 \rightarrow 0} \frac{1}{d\Sigma_0} \int_{\mathcal{V}_1} \nabla^2 u \, d\mathcal{V} = \mathbf{n}_0 \cdot \nabla u \Big|_0^1 + \hat{\nabla}_S \cdot (\delta \nabla u) = 0, \quad (\text{A } 9)$$

where $\Big|_0^1$ refers to the difference of the evaluation on the surfaces $d\Sigma_0$ and $d\Sigma_1$.

Substitution of (A 3), (A 5) and (A 9) into (A 2) leads to the linearised Robin boundary condition

$$\alpha u_0 + \beta \mathbf{n}_0 \cdot \nabla u_0 = \gamma \quad \text{at } \Sigma_0, \quad (\text{A } 10a)$$

$$\alpha(u_1 + \delta \mathbf{n}_0 \cdot \nabla u_0) + \beta[\mathbf{n}_0 \cdot \nabla u_1 + \hat{\nabla}_S \cdot (\delta \nabla u_0)] = \delta \mathbf{n}_0 \cdot \nabla \gamma \quad \text{at } \Sigma_0. \quad (\text{A } 10b)$$

Note that only \mathbf{n}_0 enters in (A 10) and \mathbf{n}_1 is not necessary in the linearisation. In the computations carried out in this work, (A 10) has been used in (3.12) and (3.13).

The system of equations (A 4) and (A 10) is the linearised counterpart of (A 1) and (A 2).

Analogously, integrating the identity $\nabla \cdot \mathcal{I} = 0$ over the volume \mathcal{V}_1 and substituting (A 6) yields to the perturbation of the normal vector

$$\mathbf{n}_1 = \hat{\nabla}_S d \quad \text{at } \Sigma_0, \quad (\text{A } 11)$$

which together with (A 7) can be used instead of (A 9).

Appendix B. Reversibilities and symmetries

Leading order creeping flow, denoted with subindex 0, is reversible. In effect, if we change the direction of the mean flow

$$J \leftarrow -J, \quad (\text{B } 1)$$

the reversed fields, denoted with the subindex R , fulfil

$$p_0(x, y, z) = -p_R(x, y, z), \quad \mathbf{v}_0(x, y, z) = -\mathbf{v}_R(x, y, z). \quad (\text{B } 2)$$

Furthermore, if the geometry exhibit symmetry with respect to the plane $x = 0$, the flow is also anti-symmetric with respect to this plane,

$$p_0(x, y, z) = -p_0(-x, y, z), \quad \mathbf{v}_0(x, y, z) = -\mathcal{S} \cdot \mathbf{v}_0(-x, y, z), \quad (\text{B } 3)$$

where $\mathcal{S} = -e_x e_x + e_y e_y + e_z e_z$ is the symmetry tensor with respect to the x -direction.

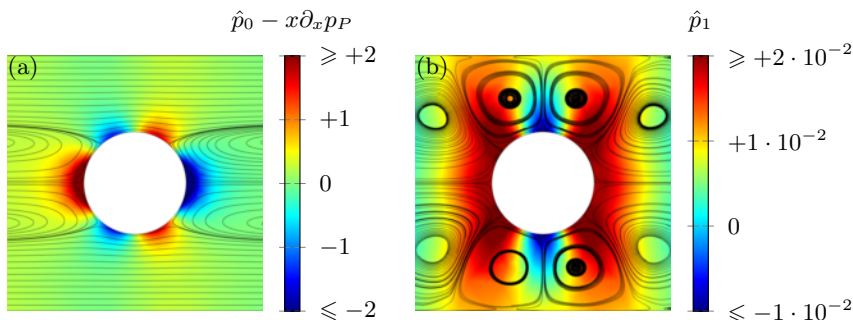


FIGURE 17. Streamlines and pressure field at the $z = 0$ symmetry plane (a) of the anti-symmetric and reversible flow \hat{p}_0 and \mathbf{v}_0 and (b) of the symmetric and anti-reversible flow \hat{p}_1 and \mathbf{v}_1 for a centred bubble of size $d = 0.4$ and with rigid surface.

Evaluating expressions (B 2) at an arbitrary plane $x = h$, dividing by h and evaluating the limit when $h \rightarrow 0$, it writes

$$p(0, y, z) = 0, \quad \partial_x \mathbf{v}(0, y, z) \cdot \mathbf{e}_x = 0, \quad \mathbf{v}(0, y, z) \cdot \mathbf{e}_y = 0, \quad \mathbf{v}(0, y, z) \cdot \mathbf{e}_z = 0 \quad (\text{B } 4)$$

Analogously, pure linear inertial or capillary correction of the creeping flow, denoted by the subindex 1, are anti-reversible. The change of direction of the mean flow (B 1) does not affect the linear correction since all non-homogeneous terms in the governing equations are quadratic in the creeping fields, \hat{p}_0 , \mathbf{v}_0 and δ_0 (if applicable) and all negative signs cancel. The anti-reversibility character is described by

$$p_1(x, y, z) = p_{AR}(x, y, z), \quad \mathbf{v}_1(x, y, z) = \mathbf{v}_{AR}(x, y, z) \quad (\text{B } 5)$$

where subindex *AR* refers to anti-reversible. In symmetric geometries, anti-reversible flows are also symmetric and fulfil

$$p_1(x, y, z) = p_1(-x, y, z), \quad \mathbf{v}_1(x, y, z) = \mathcal{S} \cdot \mathbf{v}_1(-x, y, z). \quad (\text{B } 6)$$

The limit $h \rightarrow 0$ of the evaluation of (B 6) at the arbitrary plane $x = h$ divided by h lead to the anti-symmetry conditions

$$\partial_x p(0, y, z) = 0, \quad \mathbf{v}(0, y, z) \cdot \mathbf{e}_x = 0, \quad \partial_x \mathbf{v}(0, y, z) \cdot \mathbf{e}_y = 0, \quad \partial_x \mathbf{v}(0, y, z) \cdot \mathbf{e}_z = 0. \quad (\text{B } 7)$$

Examples of both kinds of flows are depicted in fig. 17 with small numerical errors in the streamlines.

REFERENCES

- CHAN, PC-H & LEAL, LG 1979 The motion of a deformable drop in a second-order fluid. *Journal of Fluid Mechanics* **92** (01), 131–170.
- CHEN, XIAODONG, XUE, CHUNDONG, ZHANG, LI, HU, GUOQING, JIANG, XINGYU & SUN, JIASHU 2014 Inertial migration of deformable droplets in a microchannel. *Physics of Fluids* **26** (11), 112003.
- COULLETTE, C & POZRIKIDIS, C 1998 Motion of an array of drops through a cylindrical tube. *Journal of fluid mechanics* **358**, 1–28.
- COX, RG & BRENNER, H 1968 The lateral migration of solid particles in poiseuille flow-i theory. *Chemical Engineering Science* **23** (2), 147–173.
- CUBAUD, THOMAS & HO, CHIH-MING 2004 Transport of bubbles in square microchannels. *Physics of fluids* **16** (12), 4575–4585.
- DI CARLO, DINO, EDD, JON F, IRIMIA, DANIEL, TOMPKINS, RONALD G & TONER, MEHMET

- 2008 Equilibrium separation and filtration of particles using differential inertial focusing. *Analytical chemistry* **80** (6), 2204–2211.
- GÜNTHER, AXEL, KHAN, SAIF A, THALMANN, MARTINA, TRACHSEL, FRANZ & JENSEN, KLAUS F 2004 Transport and reaction in microscale segmented gas–liquid flow. *Lab on a Chip* **4** (4), 278–286.
- HO, BP & LEAL, LG 1974 Inertial migration of rigid spheres in two-dimensional unidirectional flows. *Journal of Fluid Mechanics* **65** (02), 365–400.
- HOOD, KAITLYN, LEE, SUNGYON & ROPER, MARCUS 2015 Inertial migration of a rigid sphere in three-dimensional poiseuille flow. *Journal of Fluid Mechanics* **765**, 452–479.
- KEMNA, EVELIEN WM, SCHOEMAN, ROGIER M, WOLBERS, FLOOR, VERMES, ISTVAN, WEITZ, DAVID A & VAN DEN BERG, ALBERT 2012 High-yield cell ordering and deterministic cell-in-droplet encapsulation using dean flow in a curved microchannel. *Lab on a Chip* **12** (16), 2881–2887.
- KENNEDY, MR, POZRIKIDIS, C & SKALAK, R 1994 Motion and deformation of liquid drops, and the rheology of dilute emulsions in simple shear flow. *Computers & Fluids* **23** (2), 251–278.
- LESHANSKY, AM, BRANSKY, A, KORIN, N & DINNAR, U 2007 Tunable nonlinear viscoelastic focusing in a microfluidic device. *Physical review letters* **98** (23), 234501.
- MATAS, JEAN-PHILIPPE, MORRIS, JEFFREY F & GUZZELLI, ÉLISABETH 2004 Inertial migration of rigid spherical particles in poiseuille flow. *Journal of Fluid Mechanics* **515**, 171–195.
- MCLAUGHLIN, JOHN B 1991 Inertial migration of a small sphere in linear shear flows. *Journal of Fluid Mechanics* **224**, 261–274.
- MIKAELIAN, DAVID, HAUT, BENOÎT & SCHEID, BENOIT 2015a Bubbly flow and gas–liquid mass transfer in square and circular microchannels for stress-free and rigid interfaces: Cfd analysis. *Microfluidics and Nanofluidics* **19** (3), 523–545.
- MIKAELIAN, DAVID, HAUT, BENOÎT & SCHEID, BENOIT 2015b Bubbly flow and gas–liquid mass transfer in square and circular microchannels for stress-free and rigid interfaces: dissolution model. *Microfluidics and Nanofluidics* **19** (4), 899–911.
- MORTAZAVI, SAEED & TRYGGVASON, GRÉTAR 2000 A numerical study of the motion of drops in poiseuille flow. part 1. lateral migration of one drop. *Journal of Fluid Mechanics* **411**, 325–350.
- OLIVER, DR 1962 Influence of particle rotation on radial migration in the poiseuille flow of suspensions. *Nature* **194** (4835), 1269–1271.
- PAK, ON SHUN, FENG, JIE & STONE, HOWARD A 2014 Viscous marangoni migration of a drop in a poiseuille flow at low surface pécelet numbers. *Journal of Fluid Mechanics* **753**, 535–552.
- PAMME, NICOLE 2007 Continuous flow separations in microfluidic devices. *Lab on a Chip* **7** (12), 1644–1659.
- SCHONBERG, JEFFREY A & HINCH, EJ 1989 Inertial migration of a sphere in poiseuille flow. *Journal of Fluid Mechanics* **203**, 517–524.
- SEGRÉ, G & SILBERBERG, A 1962 Behaviour of macroscopic rigid spheres in poiseuille flow part 2. experimental results and interpretation. *Journal of Fluid Mechanics* **14** (01), 136–157.
- SHIM, SUIN, WAN, JIANDI, HILGENFELDT, SASCHA, PANCHAL, PRATHAMESH D & STONE, HOWARD A 2014 Dissolution without disappearing: multicomponent gas exchange for co 2 bubbles in a microfluidic channel. *Lab on a Chip* **14** (14), 2428–2436.
- SINGH, RAJESH KUMAR, LI, XIAOYI & SARKAR, KAUSIK 2014 Lateral migration of a capsule in plane shear near a wall. *Journal of Fluid Mechanics* **739**, 421–443.
- STAN, CLAUDIU A, ELLERBEE, AUDREY K, GUGLIELMINI, LAURA, STONE, HOWARD A & WHITESIDES, GEORGE M 2013 The magnitude of lift forces acting on drops and bubbles in liquids flowing inside microchannels. *Lab on a Chip* **13** (3), 365–376.
- STAN, CLAUDIU A, GUGLIELMINI, LAURA, ELLERBEE, AUDREY K, CAVIEZEL, DANIEL, STONE, HOWARD A & WHITESIDES, GEORGE M 2011 Sheathless hydrodynamic positioning of buoyant drops and bubbles inside microchannels. *Physical Review E* **84** (3), 036302.
- SUBRAMANIAN, R. SHANKAR 1983 Thermocapillary migration of bubbles and droplets. *Advances in Space Research* **3** (5), 145 – 153.
- TACHIBANA, M 1973 On the behaviour of a sphere in the laminar tube flows. *Rheologica Acta* **12** (1), 58–69.

- TAKEMURA, FUMIO, MAGNAUDET, JACQUES & DIMITRAKOPOULOS, PANAGIOTIS 2009 Migration and deformation of bubbles rising in a wall-bounded shear flow at finite reynolds number. *Journal of Fluid Mechanics* **634**, 463–486.
- VASSEUR, P & COX, RG 1976 The lateral migration of a spherical particle in two-dimensional shear flows. *Journal of Fluid Mechanics* **78** (02), 385–413.
- VASSEUR, P & COX, RG 1977 The lateral migration of spherical particles sedimenting in a stagnant bounded fluid. *Journal of Fluid Mechanics* **80** (3), 561–591.
- YANG, BH, WANG, J, JOSEPH, DD, HU, HOWARD H, PAN, T-W & GLOWINSKI, R 2005 Migration of a sphere in tube flow. *Journal of Fluid Mechanics* **540**, 109–131.
- ZHOU, HUA & POZRIKIDIS, C 1993 The flow of suspensions in channels: single files of drops. *Physics of Fluids A: Fluid Dynamics* **5** (2), 311–324.